Original Article

MOLECULAR
METABOLISM

NIK/MAP3K14 in hepatocytes orchestrates NASH to hepatocellular carcinoma progression via JAK2/STAT5 inhibition

Anna Juliane Vesting [1], Alexander Jais [1,2], Paul Klemm [1], Lukas Steuernagel [1], Peter Wienand [1], Morten Fog-Tonnesen [3], Henning Hvid [4], Anna−Lena Schumacher [5], Christian Kukat [5], Hendrik Nolte [5], Theodoros Georgomanolis [6], Janine Altmüller [6], Manolis Pasparakis [7], Andreas Schmidt [7], Marcus Krüger [7], Marc Schmidt Supprian [8], Ari Waisman [9], Beate Katharina Straub [10], Nathanael Raschzok [11], Michel Bernier [12], Andreas L. Birkenfeld [13], Nadine Hövelmeyer [9], Jens C. Brüning [1], F. Thomas Wunderlich [1,*]

ABSTRACT

Objective: Nonalcoholic fatty liver disease (NAFLD) ranges from steatosis to nonalcoholic steatohepatitis (NASH), which often progresses to hepatocellular carcinoma (HCC) through a largely undefined mechanism. NASH and HCC depend on inflammatory signaling, whose master regulator is the NFκB transcription factor family, activated by canonical and non-canonical pathways.

Methods: Here, we investigated non-canonical NFκB-inducing kinase (NIK/MAP3K14) in metabolic NASH, NASH to HCC transition, and DEN-induced HCC. To this end, we performed dietary and chemical interventions in mice that were analyzed via single nucleus sequencing, gene expression and histochemical methods. Ultimately, we verified our mouse results in human patient samples.

Results: We revealed that hepatocyte-specific NIK deficiency (NIKLKO) ameliorated metabolic NASH complications and reduced hepatocarcinogenesis, independent of its role in the NFκB pathway. Instead, hepatic NIK attenuated hepatoprotective JAK2/STAT5 signaling that is a prerequisite for NASH and NASH to HCC progression in mice and humans.

Conclusions: Our data suggest NIK-mediated inhibitory JAK2 phosphorylation at serine 633 that might be amenable for future therapeutic interventions in patients.

1. INTRODUCTION

The global escalating obesity pandemic has led to a spike in obesity-related diseases such as cardiovascular disease and nonalcoholic fatty liver disease (NAFLD) [1−4]. NAFLD is a spectrum of chronic liver diseases ranging from simple hepatic triglyceride accumulation and hepatic steatosis (nonalcoholic fatty liver) to progressing liver injury and inflammation, a condition known as nonalcoholic steatohepatitis (NASH) [5]. Several studies have demonstrated that NASH can sequentially progress to fibrosis, cirrhosis, and hepatocellular carcinoma (HCC) [6]. While in Asia and Africa hepatitis B and/or C virus infections account for the majority of HCC cases, in developed countries the proportion of HCC related to NASH increases exponentially resulting from the accelerating obesity pandemic.

[1]Max Planck Institute for Metabolism Research, Gleueler Strasse 50, 50931 Cologne, Germany, Center for Endocrinology, Diabetes and Preventive Medicine (CEDP), University Hospital Cologne, Kerpener Strasse 26, 50924 Cologne, Germany, Excellence Cluster on Cellular Stress Responses in Aging Associated Diseases (CECAD) and Center of Molecular Medicine Cologne (CMMC), University of Cologne, Cologne, Germany [2]Helmholtz Institute for Metabolic, Obesity and Vascular Research (HI-MAG), 04103 Leipzig, Germany [3]Global Drug Discovery, Novo Nordisk A/S, Novo Nordisk Park 1, 2760 Maaloev, Denmark [4]Pathology & Imaging, Novo Nordisk A/S, Novo Nordisk Park 1, DK-2760 Maaloev, Denmark [5]Max Planck Institute for Biology of Ageing, Joseph-Stelzmann-Str. 9b, 50931 Cologne, Germany [6]University of Cologne, Cologne Center for Genomics, Cologne, Germany [7]Institute for Genetics, University of Cologne, 50674 Cologne, Germany, Cologne Excellence Cluster on Cellular Stress Responses in Aging-Associated Diseases (CECAD), University of Cologne, 50931 Cologne, Germany, Center for Molecular Medicine Cologne (CMMC), University of Cologne, 50931 Cologne, Germany [8]Institute of Experimental Hematology, TranslaTUM, Klinikum rechts der Isar der Technischen Universität München, 81675 Munich, German Cancer Consortium (DKTK) and German Cancer Research Center (DKFZ) 69120 Heidelberg, Germany [9]Institute for Molecular Medicine, Research Center for Immunotherapy, University Medical Center of the Johannes Gutenberg-University Mainz, 55131 Mainz, Germany [10]Institute of Pathology, University Medical Centre of the Johannes Gutenberg-University Mainz, 55131 Mainz, Germany [11]General, Visceral, and Transplantation Surgery, Charité-University School of Medicine, 13353 Berlin, Germany− Universitätsmedizin Berlin, corporate member of Freie Universität Berlin and Humboldt-Universität zu Berlin, Department of Surgery, Experimental Surgery, Campus Charité Mitte | Campus Virchow-Klinikum, Berlin, Germany and Berlin Institute of Health at Charité — Universitätsmedizin Berlin, BIH Academy, Clinician Scientist Program, Berlin, Germany [12]Translational Gerontology Branch, National Institute on Aging, National Institutes of Health, Baltimore, MD, USA [13]Internal Medicine IV, Clinic of Diabetology, Endocrinology, Nephrology, Internal medicine IV, University Hospital and Faculty of Medicine of the Eberhard Karls University Tübingen, 72016 Tübingen, Germany and Institute of Diabetes Research and Metabolic Diseases, Helmholtz Zentrum München an der Uniklinik Tübingen, Deutsches Zentrum für Diabetesforschung (DZD), Germany

*Corresponding author. E-mail: Thomas.wunderlich@sf.mpg.de (F.T. Wunderlich).

Received July 21, 2022 • Revision received October 21, 2022 • Accepted October 28, 2022 • Available online 7 November 2022

https://doi.org/10.1016/j.molmet.2022.101626

Original Article

Despite the increasing evidence of the sequential development of chronic steatohepatitis and fibrosis ultimately leading to cirrhosis and HCC, the cellular and molecular pathomechanisms underlying NASH and NASH-induced HCC are largely unknown [7]. In NASH and HCC chronic inflammation promotes disease progression via triggering a vicious cycle of cell death, hyperproliferation, and escape from cell cycle control, ultimately resulting in tumor formation [8]. Although impairment of growth hormone-induced STAT5 has been shown to be a critical step in HCC development, it is not yet clear how inflammation impacts this signaling pathway to promote NASH and HCC development [9].

NFκB is the master regulator of inflammation which was shown to be altered in numerous diseases [10]. While the canonical NFκB1 pathway mediates inflammatory processes, e.g. in response to TNFα, non-canonical NFκB2 signaling has mainly been studied in orchestrating immune cell differentiation and secondary lymphoid organogenesis [11]. We and others have demonstrated the importance of canonical NFκB signaling in HCC development [12—16]. Importantly, ligands that act on LTβR or Fn14 are able to activate both canonical as well as non-canonical NFκB signaling. Receptor engagement inactivates intracellular TRAF2/3-cIAP ubiquitination complex to stabilize the central non-canonical NFκB-inducing kinase NIK/MAP3K14 (Figure 1A) [17]. NIK in turn activates IKK1 that subsequently phosphorylates p100, resulting in its partial proteasomal degradation to p52 [18]. Heterodimeric p52-Rel-B represents the active non-canonical NFκB transcription factor complex that translocates into the nucleus to regulate target gene expression. Despite the detailed molecular characterization of the NFκB2 pathway, the function of non-canonical NFκB signaling in the liver might be diverse and disease dependent. Apart from its function in proliferation and cell survival [19—24], overexpression and aberrant NIK activation have been shown to not only cause severe liver injury but also to promote liver regeneration upon partial hepatectomy [25,26]. Furthermore, NIK inactivation prevented not only the development of diet-induced hyperglycemia but also ameliorated hepatic lipid accumulation in high fat diet-fed mice [26]. However, despite these extensive phenotypical characterizations of hepatic NIK, the molecular function of NIK in NASH and HCC still remains elusive.

Thus, we investigated hepatocyte-specific *NIK* knockout (*NIK^{LKO}*) mice in a metabolic NASH model, a NASH to HCC transition model, and a diethylnitrosamine (DEN)-induced HCC model. Our results reveal that hepatic NIK promotes insulin resistance and hepatic lipid accumulation in metabolic NASH whereas hepatic NIK induces tumor development in NASH to HCC transition as well as in DEN-induced HCC models. Mechanistically, NIK impairs the activation of the JAK2/STAT5 signaling axis in all three disease models. Furthermore, we verify the inhibitory action of NIK on JAK2/STAT5 signaling in human HCC development that might be amenable for future therapeutic treatments of patients suffering from NASH and HCC.

2. RESULTS

In NASH, chronic liver inflammation triggers liver damage and sustained hepatic fibrogenesis ultimately resulting in the progression from NASH to HCC. This disease progression is partially mediated by inflammatory signaling such as the NFκB pathway. The NFκB transcription factor family is activated by canonical and non-canonical pathways. The non-canonical NFκB cascade critically depends on NIK whose function has not yet been investigated in the sequential development from NASH to HCC. To unravel the role of *NIK* in NASH and in the progression of NASH to HCC, we generated hepatocyte-

specific *NIK*-deficient mice (*NIK^{LKO}*) by crossing mice carrying a loxP-flanked *NIK* allele (*NIK^{fl/fl}*) [27] with *Alfp-Cre* mice [28]. *NIK^{LKO}* mice were born at expected Mendelian ratio and showed no obvious phenotype. The assessment of hepatocyte-specific *NIK* inactivation via qPCR revealed not only significantly reduced expression of *NIK* mRNA in the liver of *NIK^{LKO}* animals but also impaired p100 to p52 processing in *NIK*-deficient primary hepatocytes (Figure S1A-B). Thus, our mouse model of hepatic *NIK* deficiency allows for investigating the impact of NIK in NASH and in NASH to HCC transition.

2.1. Hepatocyte-specific *NIK* deficiency ameliorates insulin sensitivity, glucose homeostasis, and hepatic lipid accumulation in mice fed a metabolic NASH diet

Mice fed a high-fat, high-fructose diet supplemented with trans-fat and cholesterol (NASH diet) manifest the metabolic impairments of human NASH characterized by the development of insulin resistance and hepatic lipid accumulation. However, mice only develop mild to no fibrosis and show no alterations in collagen deposition and extracellular matrix remodelling [29,30].

To examine the metabolic functions of *NIK* in NASH, we exposed 6 weeks old control and *NIK^{LKO}* mice to the NASH diet for 20 weeks (Figure 1B). While body weight gain and body composition were largely unaltered (Figure S 1C-E), *NIK^{LKO}* mice showed improved insulin sensitivity, glucose tolerance, and reduced circulating insulin levels thus indicating improved insulin sensitivity in NASH (Figure 1C—E). Moreover, hepatic *NIK* deficiency prevented ectopic lipid accumulation in the liver upon NASH diet feeding. Macroscopic inspection of the liver revealed that livers from control animals displayed clear signs of ectopic fat deposition, whereas *NIK^{LKO}* livers resembled that of lean animals (Figure 1F). Quantification of liver Oil red O stainings and hepatic triglyceride assays confirmed reduced lipid accumulation in *NIK^{LKO}* mice compared to control mice (Figure 1G—H).

While liver mass, hepatic inflammation, and immune cell infiltration were largely unaltered between the groups, the white adipose tissue mass was decreased in *NIK^{LKO}* mice. Consistent with improved insulin sensitivity, white adipose tissue of *NIK^{LKO}* mice showed a reduction in inflammation and of crown-like structures as demonstrated by qPCR and immunohistochemistry (Figure S1F-K).

However, careful histological examination of livers showed no differences in fibrotic collagen (Pico Sirius red) and stellate cells to myofibroblasts differentiation (α-SMA staining) between the groups, which is in line with unaltered expression of mediators of extracellular matrix remodelling (Figure S1L-N). Thus, mice with hepatocyte-specific *NIK* deficiency show improved metabolic parameters in NASH, but largely unaltered hepatic inflammation and fibrosis.

To get first insights into the hepatocyte-specific *NIK*-dependent mechanism of ectopic lipid deposition in NASH, we performed single nuclei RNA sequencing (snRNAseq) from livers of control and *NIK^{LKO}* animals (n = 1 each). Integration and clustering of single nuclear transcriptomic profiles identified 11 cell clusters, which were assigned to different cell types based on cell type-specific markers (Supplementary Table 1). The clusters were equally distributed between the genotypes and were classified into hepatocytes, activated hepatic stellate cells, two distinct B cell clusters, a cholangiocyte cluster, endothelial cell cluster, two distinct macrophage clusters, myofibroblast cluster, T cells, and doublets (Figure 1I). While most hepatocyte clusters were evenly distributed between control and NIK knock out liver, cell counts of Chrm3and differentiating clusters were reduced in *NIK*-deficient hepatocytes — the latter exhibits gene expression related to cell cycle and proliferation (Figure 1O, Supplementary Table 1). The decreased proliferation in the livers of
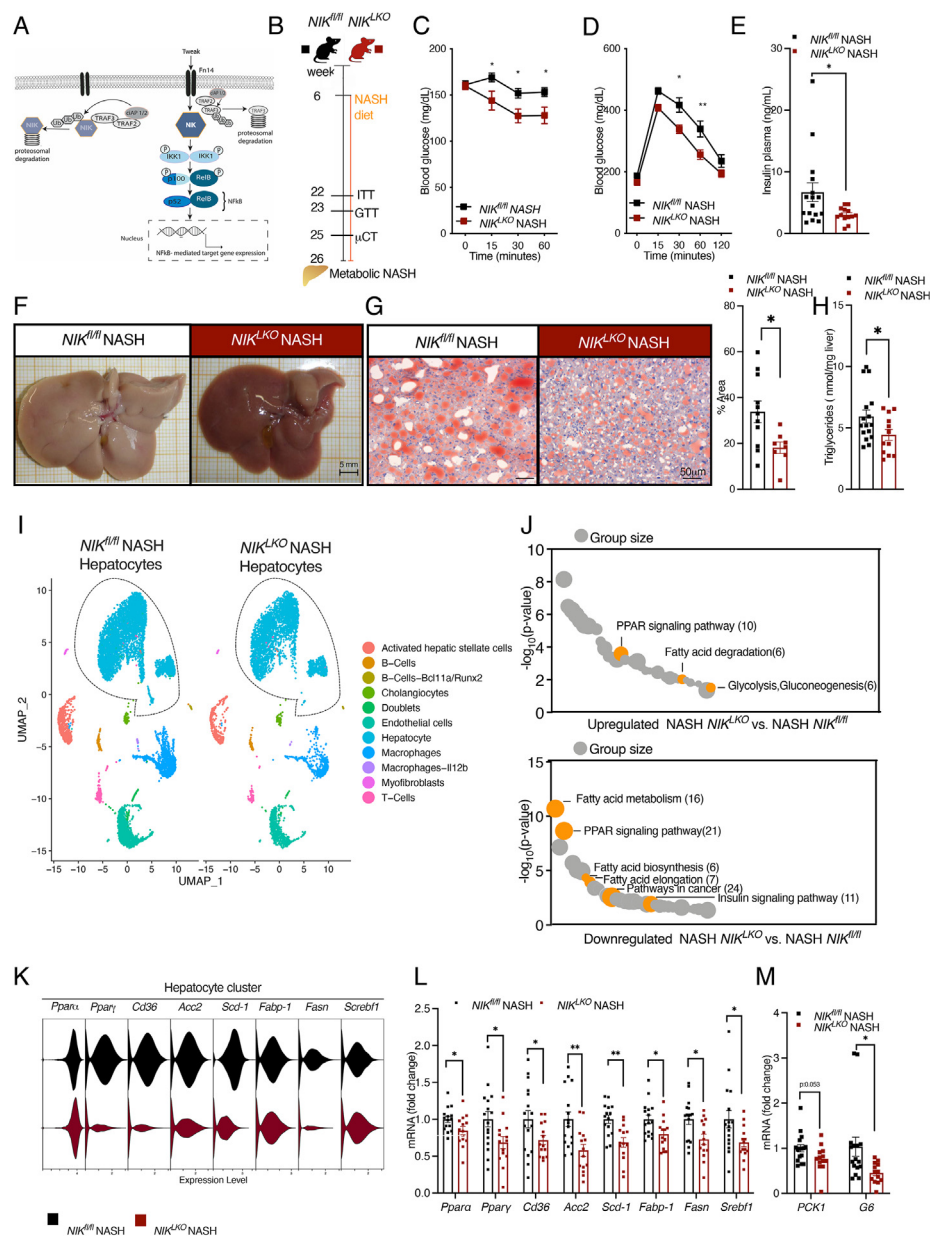
Figure 1: Hepatocyte-specific *NIK* deficiency ameliorates insulin sensitivity, glucose homeostasis and hepatic lipid accumulation in mice fed a metabolic NASH diet. (A) Schematic representation of non-canonical NFκB signaling. The non-canonical NFκB signaling pathway is activated by a specific subset of receptor and ligands, e.g. TWEAK and its hepatic Fn14 receptor. In the absence of a stimulus, NIK is degraded whereas in the presence of TWEAK the E3 ubiquitin ligase complex is disrupted resulting in the degradation of TRAF3. Stabilization and accumulation of NIK results in phosphorylation of IKK1, which in turn phosphorylates p100 resulting in its partial proteasomal degradation to p52. Subsequently the p52/RELB NFκB complex translocates into the nucleus to induce target gene expression. (B) Time course of NASH model used in this study. Male NIK$^{fl/fl}$ and NIK^{LKO} mice were fed a NASH diet for 20 weeks. With 22 and 23 weeks of age ITT and GTT analysis was performed. Body composition was assessed at 25 weeks. (C) Insulin tolerance test in 22 weeks old NASH-fed NIK$^{fl/fl}$ and NIK^{LKO}, (n = 17/14). (D) Glucose tolerance test in 23 weeks old NASH-fed NIK$^{fl/fl}$ and NIK^{LKO} NIK^{LKO} (n = 17/12). (E) Basal random-fed insulin levels in 26 weeks old NASH-fed NIK$^{fl/fl}$ and NIK^{LKO} (NIK^{LKO} 3.04 ± 0.32 vs. control 6.69 ± 1.51, p ≤ 0.042) (n = 16/13). (F) Representative images of NASH livers of 26 weeks old NIK$^{fl/fl}$ and NIK^{LKO} mice, scale bar 5 mm. (G) Representative images of Oil-Red- O staining of NASH livers of 26 weeks old NIK$^{fl/fl}$ and NIK^{LKO} mice (NIK^{LKO} 18.17 ± 2.50 vs. control 33.79 ± 4.70, p ≤ 0.017) and corresponding quantification (n = 11/8), scale bar 50 mm. (H) Triglyceride levels in NASH livers of 26 weeks old NIK$^{fl/fl}$ and NIK^{LKO} mice (NIK^{LKO} 4.23 ± 0.45 vs. control 5.89 ± 0.56, p ≤ 0.044) (n = 16/13). (I) UMAP visualization of annotated nuclei in NIK$^{fl/fl}$ and NIK^{LKO} NASH liver samples. (J) GSEA analysis of NASH-fed NIK$^{fl/fl}$ and NIK^{LKO} hepatocyte molecular signatures. Terms are sored according to their P-value. Notable terms are highlighted; P-values are derived from Fisher's exact test and pass Benjamini-Hochberg corrected P < 0.05. (K) Violin blots of lipogenic transcription factor peroxisome proliferator-activated receptor gamma (PPARg) and peroxisome proliferator-activated receptor gamma alpha (PPARa), the fatty acid transporter CD36 and fatty acid-binding protein (Fabp-1), of hepatic de novo lipogenesis acetyl-CoA carboxylase2 (Acc-2), fatty acid synthase (Fasn), stearoyl-CoA 1 (SCD1), and Sterol regulatory element-binding transcription factor 1(Srebf1) from isolated single nuclei of the hepatocyte cluster. (L) qPCR analysis of lipogenic transcription factor peroxisome proliferator-activated receptor gamma (*PPARg*) and peroxisome proliferator-activated receptor gamma alpha (*PPARa)*, the fatty acid transporter CD36 and fatty acid-binding protein (Fabp-1), of hepatic de novo *lipogenesis* acetyl-CoA carboxylase2 (*Acc-2*), fatty acid synthase (*Fasn*), stearoyl-CoA 1 (SCD1), and Srebf1 in NASH livers of 26 weeks old NIK$^{fl/fl}$ and NIK^{LKO} mice (n = 16/13). M) qPCR analysis of phosphoenolpyruvate carboxykinase 1 (*Pck-1*) and glucose 6-phosphatase (*G6*) Srebf1 in NASH livers of 26 weeks NIK$^{fl/fl}$ and NIK^{LKO} (n = 16/13). Data are presented as mean ± SEM; *p ≤ 0.05, **p ≤ 0.01. Statistical analyses were performed using Student's *t*-test (A, B) and two-way ANOVA plus Fisher's LSD test.

NIK^{LKO} mice was verified by reduced Ki-67 and increased cleaved caspase 3 reactivity in IHC, but in the absence of liver damage (Figure S1P-R). To determine differences in hepatocyte-specific gene expression, we performed unbiased KEGG pathway analysis of altered gene expression from all hepatocyte clusters between the genotypes. This analysis identified fatty acid metabolism and PPAR signaling as the main affected pathways downregulated in *NIK*-deficient hepatocytes (Figure 1J, Supplementary Table 2). In line with the single nuclei sequencing results, expression of *Pparα* and *Pparγ* as well as their target genes *Fasn, CD36, Acc-2, Scd-1, Fabp-1* and *Srebf1* were all reduced in *NIK*-deficient livers fed the NASH diet (Figure 1K,L). Although fatty acid transporter CD36 was reduced in NIK^{LKO} livers, there were neither alterations in plasma triglycerides nor free fatty acids (Figure S1ST). Furthermore, alterations in insulin signaling and gluconeogenesis could be verified by reduced expression of gluconeogenic genes *Pck1* and *G6pc* (Figure 1M).

Taken together, our experiments reveal that hepatocyte-specific *NIK* deficiency improves insulin sensitivity and prevents hepatic lipid accumulation by altered PPAR signaling. Importantly, mice exposed to the control diet to NASH revealed no differences between the genotypes, thereby demonstrating that hepatic NIK deficiency prevented NASH complications only in the dietary intervention model but not under steady state conditions (Figure S1U-AC).

2.2. NIK^{LKO} mice show reduced liver tumors in NASH to HCC transition

The metabolic NASH diet recapitulates metabolic alterations but in the absence of fibrosis. To study the role of *NIK* in a fibrosis model of NASH to HCC transition, NIK^{LKO} and control mice were exposed to a choline-deficient, L-amino acid-defined HFD diet for 20 weeks (CDAA) or to a control diet with choline (CSAA) (Figure 2A, Figure S2A). No large alterations in body weight gain and body composition, epigonadal fat pad and liver weights as well as insulin and glucose tolerance were observed in CDAA cohorts, but improved glucose tolerance in CSAA fed NIK^{LKO} mice consistent with our previous finding (Figure S2B-G). While liver damage was similar between the genotypes on fibrosis diet, NIK^{LKO} exhibited reductions in the systemic level of IL-6, CCL3, and RANTES as examined by multiplex ELISA as well as decreased hepatic mRNA expression of *Tnfα* and *Il-6* (Figure S2H-L). Nevertheless, fibrosis development was unaffected by hepatic NIK deficiency as no differences in extracellular matrix gene expression profile, collagen deposition as assessed by Pico Sirius staining as well as unaltered hepatic stellate cell activation were observed between the genotypes (Figure S2M—O). While hepatic immune cell infiltration was largely unaffected, qPCR and IHC revealed an increase of Trem2+ macrophages that try to combat fibrosis (Figure S2P-S). Nevertheless, hepatic NIK deficiency fails to largely affect fibrosis and inflammation in the CDAA mouse model.

However, all control mice developed liver tumors at the end of the study, whereas only 47.05% of NIK^{LKO} mice had tumors (Figure 2B). Tumor nodules from both genotypes showed characteristics of regenerative hyperplasia progressing to adenoma in the absence of HCC. NIK^{LKO} livers demonstrated less tumor nodules in total as well as when stratified into small and larger nodules (Figure 2C). Reduced liver tumorigenesis in NIK^{LKO} mice could be attributed to decreased proliferation as evidenced by PCNA immunoreactivity but in the presence of unaltered apoptosis between the genotypes (Figure S2TU).

To examine the molecular mechanism leading to reduced liver tumorigenesis in NIK^{LKO} mice upon CDAA HFD diet, we performed

snRNAseq isolated from $NIK^{fl/fl}$ and NIK^{LKO} mice (Figure 2D, Figure S2V). SnRNAseq identified evenly distributed hepatocyte clusters between the genotypes. KEGG pathway analysis revealed similar terms when compared to previous metabolic NASH experiment with PPAR signaling, fatty acid degradation, and JAK-STAT as major pathways regulated in NIK-deficient hepatocytes (Figure 2E)

Collectively, these data reveal that hepatocyte-specific *NIK* deficiency in a fibrosis model of NASH to HCC transition decreased liver tumorigenesis without altering fibrosis. Strikingly, snRNAseq experiments revealed similar regulated hepatocyte-specific pathways in both the fibrosis model and the metabolic NASH model.

2.3. Hepatic *NIK* deficiency reduces DEN-induced HCC

Given that hepatic NIK deficiency ameliorated metabolic and malignant NASH complications in dietary intervention experiments (metabolic NASH and CDAA diets), we aimed at investigating the role of *NIK* in HCC development. To this end, NIK^{LKO} and control mice were subjected to the well-established DEN-induced HCC model that shows only moderate fibrosis in cancer progression [31]. Since hepatic lipid accumulation and/or metabolic alterations can affect HCC progression, we synchronized control and NIK^{LKO} mice in the DEN experiment by exposing mouse cohorts to a control diet low in fat content (CD) (Figure 2F). Body weight gain was unaltered between the groups and insulin sensitivity as well as glucose tolerance were largely unaffected in NIK^{LKO} mice (Figure S3A-C). Liver weight, fat mass, and body composition in NIK^{LKO} mice were comparable to control mice in the presence of unaltered hepatic lipid accumulation (Figure S3D-I). Thus, feeding a low-fat control diet averted the metabolic phenotype in hepatic *NIK*-deficient mice in DEN-induced HCC.

Strikingly, hepatic *NIK* deficiency in the DEN model resulted in significant reduction in the number of HCC tumors (Figure 2G—H). Stratification of tumors by size revealed the development of predominantly smaller tumors in NIK^{LKO} livers (Figure 2H,I), coincident with reduced Ki67 immunoreactivity, while the proapoptotic caspase 3 activity as well as liver damage were unaffected (Figure S3J-L). Because the tumor microenvironment is a critical determinant in HCC progression, we performed qPCR and ELISA analyses of control and NIK-deficient liver to evaluate the HCC tumor microenvironment, and found similar macrophage and T cell signatures and cytokine levels in the two cohorts (Figure S3M-Q). In addition, mRNA and protein expression of the hepatic *NIK* inducers TWEAK/Fn14 and LIGHT/HVEM were unaltered (Figure S3R-T). Therefore, these experiments reveal an overall improvement of DEN-induced HCC development in hepatic *NIK*-deficient mice in the absence of metabolic and tumor microenvironment alterations indicating that the reduced HCC burden in NIK^{LKO} mice can be directly attributed to hepatocyte-intrinsic *NIK* deficiency.

To gain insights into the hepatocyte-specific mechanism of *NIK* action in HCC development, we performed snRNAseq experiments (Figure 2J). Since we observed an evenly distributed clustering between $NIK^{fl/fl}$ and NIK^{LKO} mice including the presence of all hepatocyte and tumor microenvironment cell clusters, we focused on gene expression altered in control and *NIK*-deficient hepatocytes (Figure 3U, Figure 2J—K). Again, we identified PPAR signaling and downstream fatty acid metabolism amongst the most down-regulated pathways in NIK^{LKO} HCC livers (Figure 2K). In line with the outcome of snRNAseq from CDAA diet, JAK-STAT signaling was upregulated in *NIK*-deficient hepatocytes. Thus, even under CD low fat diet condition that averted a metabolic phenotype in NIK^{LKO} mice, PPAR and downstream signalling were similarly regulated in all three disease models. Although JAK-
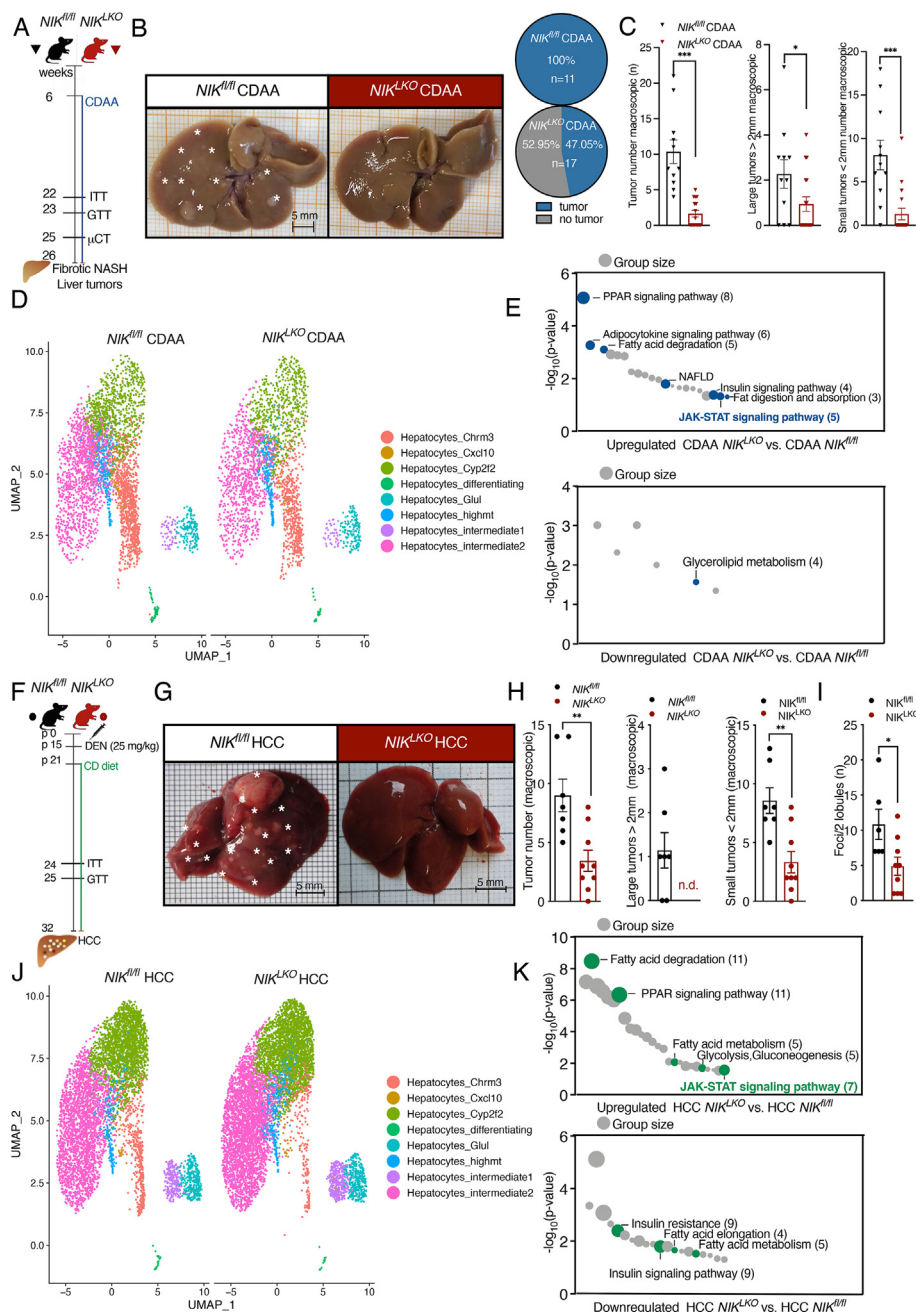
Figure 2: *NIK^LKO* mice show reduced liver tumors in the NASH to HCC progression model and Hepatic *NIK* deficiency reduces DEN-induced HCC. A) Time course of NASH to HCC transition model used in this study. Male *NIK^fl/fl* and *NIK^LKO* mice were fed a CDAA diet for 20 weeks. With 22 and 23 weeks of age ITT and GTT analysis was performed. Body composition was assessed at 25 weeks. B) Representative images of CDAA livers of 26 weeks old *NIK^fl/fl* and *NIK^LKO* mice, scale bar 5 mm and distribution of tumor incidences of *NIK^fl/fl* and *NIK^LKO* mice. C) Quantification of total macroscopic tumor burden determined by visual inspection of 26 weeks old NASH *NIK^fl/fl* and *NIK^LKO* mice (*NIK^LKO* 1.625 ± 0.47 vs. control 10.36 ± 1.67, p ≤ 4.10 E^{−06}) (n = 11/16). Quantification of macroscopic large (>2 mm) tumor multiplicity in NASH-fed *NIK^fl/fl* and *NIK^LKO* mice (*NIK^LKO* 0.94 ± 0.33 small tumors vs. control 2.27 ± 0.63, p ≤ 0.0503) (n = 11/17). Quantification of macroscopic small (<2 mm) tumor multiplicity (*NIK^LKO* 1.29 ± 0.66 small tumors vs. control 8.09 ± 1.69, p ≤ 0.0002). (n = 11/17). D) UMAP visualization of annotated nuclei in *NIK^fl/fl* and *NIK^LKO* CDAA liver samples. E) GSEA analysis of CDAA-fed *NIK^fl/fl* and *NIK^LKO* hepatocyte molecular signatures. Terms are sorted according to their P-value. Notable terms are highlighted; P-values are derived from Fisher's exact test and pass Benjamini-Hochberg corrected P < 0.05. F) Time course of DEN experiment used in this study. Male *NIK^fl/fl* and *NIK^LKO* mice were *i.p.* injected with DEN (25 mg/kg) at p15 and fed a control diet (CD) for 30 weeks. With 24 and 25 weeks of age ITT and GTT analysis was performed. The tumor burden was analyzed at 32 weeks of age. G) Representative images of HCC livers of 32 weeks old *NIK^fl/fl* and *NIK^LKO* mice, scale bar 5 mm. H) Quantification of total macroscopic tumor burden determined by visual inspection of 32 weeks old DEN-injected *NIK^fl/fl* and *NIK^LKO* mice (*NIK^LKO* 3.25 ± 0.99 vs. control 9.50 ± 1.52, p ≤ 0.0037) (n = 7/8). D) Quantification of macroscopic large (>2 mm) tumor multiplicity in CD-fed *NIK^fl/fl* and *NIK^LKO* mice (n = 7/8). E) Quantification of macroscopic small (<2 mm) tumor multiplicity (*NIK^LKO* 8.57 ± 1.08 small tumors vs. control 3.12 ± 1.00, p ≤ 0.0028). (n = 7/8). I) Assessment of tumor number per 2 lobules determined by a pathologist (*NIK^LKO* 4.88 ± 21.29 vs. control 10.83 ± 2.15 p ≤ 0.0254) (n = 7/8). J) UMAP visualization of annotated nuclei in NIK^fl/fl and NIK^LKO DEN-induced liver samples. K) GSEA analysis of *NIK^fl/fl* and *NIK^LKO* liver molecular signatures. Terms are sored according to their P-value. Notable terms are highlighted; P-values are derived from Fisher's exact test and pass Benjamini-Hochberg corrected P < 0.05. Data are presented as mean ± SEM; *p ≤ 0.05, **p ≤ 0.01. Statistical analyses were performed using Student's *t*-test.

STAT was only altered in the NASH to HCC transition and HCC models, it might also play a critical role in *NIK*-mediated steatosis in metabolic NASH model.

2.4. Hepatic NIK specifically blunts JAK2/STAT5 activation

Our extensive investigations of the role of *NIK* in metabolic NASH, NASH to HCC transition and DEN-HCC have revealed metabolic improvements and reduced liver tumorigenesis in hepatocyte-specific *NIK^LKO^* mice. To identify a common progressing mechanism of *NIK* action in all three disease models, we performed KEGG pathway analysis of differential hepatocyte-specific gene expression from newly combined snRNAseq data between all control and *NIK*-deficient hepatocytes. This analysis revealed once again that PPAR and insulin signaling as well as NAFLD were along significantly regulated pathways in the absence of *NIK* (Figure 3A). However, gene expression of typical PPAR target genes in the absence of NIK was only affected in NASH, but not or opposite in CDAA and HCC conditions (Figure 1KL, Figure S4A).

Surprisingly, JAK-STAT signaling was also amongst the significantly altered hepatocyte KEGG pathway terms and showed up in 3 out of 4 KEGG pathways (all, CDAA and HCC - not NASH), but neither NFκB nor inflammatory pathways (Figure 3AB, Supplementary Table 2). When we filtered for JAK-STAT molecules from the three models, *Igf1*, *Socs2*, *Onecut1*, *Prlr*, *Lifr* and *IL-6Rα* were regulated in all models (Figure 3C). Notably, *Igf1*, *Socs2*, *Onecut1* and *Prlr* are downstream targets of STAT5 signaling whereas *Lifr* and *IL-6Rα* are receptors that activate STAT3. Furthermore, when separating STAT5 and STAT3 molecules altered in only two or one model revealed more altered STAT5 than STAT3 factors in the absence of NIK. To evaluate which STAT transcription factor might be regulated by *NIK*, we performed Western blot analyses of steady state activated (phosphorylated) STAT1, STAT3 and STAT5 in livers from the three disease models. While STAT1 and STAT3 activation were largely unaltered, we observed enhanced STAT5 phosphorylation at Tyrosine 694 in all *NIK*-deficient mouse livers (Figure 4B-G; Figure 3D—F). In contrast, hepatic STAT5 phosphorylation was almost absent in control mice. To corroborate this finding, immunohistochemistry against active nuclear STAT5 was performed on liver sections confirming strong STAT5 activation in the absence of *NIK* (Figure 3G—I). Furthermore, investigating STAT5 target genes in snRNAseq as well as confirmation by qPCR and ELISA in the three models revealed increased STAT5 signaling in the absence of *NIK* (Figure S4HI). In primary hepatocytes, the effect of *NIK* deficiency on STAT5 target gene expression was not so intense, but could be in part affected by supplementation of a STAT5 inhibitor (Figure S4J). However, in the investigation of microarray gene expression between control and *NIK^LKO^* HCC livers revealed that the strongest regulated genes in *NIK^LKO^* livers were the well-characterized STAT5 target genes *Oncecut1*, *Cish*, *Socs2* and *Bcl6* (Figure 3J). In the liver, STAT5 signaling induces expression of hepatoprotective *Socs2*, *Onecut1* and *Cish,* but also represses *Bcl6* mainly in response to GH action. STAT5 and BCL6 are both transcription factors that share a common binding site to act opposite on gene expression [32—34]. To discriminate between STAT5-regulated and non-regulated genes among the 1507 significantly regulated genes, we performed a STAT5 binding motif search in the 2 kb upstream region in our dataset. Strikingly, this search identified STAT5 binding motifs in 33% (500 out of 1507) of differentially regulated genes where some genes such as *Cish* contained up to 4 STAT5 binding motifs (Figure 3K). Concomitantly, we screened for p52/RELB binding motifs to identify NFκB-regulated transcripts (Figure S4K). However, only 49 out of 1507 genes exhibited non-canonical NFκB2 p52/RELB binding sites (only 3% of

regulated genes). Thus, these data not only reveal *NIK* acting on STAT5, but also indirectly exclude non-canonical NFκB2-mediated gene expression in HCC. To confirm that hepatic *NIK* acts independent of downstream NFκB2 signaling to regulate STAT5, we performed pSTAT5 IHC on HCC sections from control and *IKK1^LKO^* mice that demonstrated similarly blunted STAT5 activation (Figure S4L). In line with this finding, *IKK1*-deficient mouse embryonic fibroblasts (MEFs) reacted similar in growth hormone/TWEAK-stimulated STAT5 activation experiments (Figure S4M).

STAT5 signaling prevents cell cycle progression by regulation of Cdkn gene expression. *Cdkn1b* and *Cdkn2a* [35,36] normally downregulated in HCC, were upregulated in *NIK*-deficient HCC livers indicating a block in cell cycle progression (Figure S4N). To examine compensatory proliferation and cell cycle progression, we investigated 8 weeks old control and *NIK^LKO^* mice in an acute DEN experiment by injecting a sublethal dose of DEN. Here, *NIK^LKO^* mice showed reduced liver damage 2 days *p.i.* and subsequently decreased compensatory proliferation 3 days *p.i.* (Figure S4OP). Consistently, while control mice increased *Cdkn* gene expression 2 days p.i. at highest liver damage, this was blunted in *NIK^LKO^* mice (Figure S4Q-T). We also determined hepatoprotective STAT5 target genes in this experiment revealing that neither control nor *NIK^LKO^* mice regulated *Onecut1, Cish* and *Igf1* expression during acute DEN experiments (Figure S4U-W).

Taken together, these experiments reveal hepatic STAT5 as the key molecular signaling pathway affected by *NIK,* independent of downstream non-canonical NFκB2 signaling in the three chronic progressing liver disease models but not in acute DEN and hepatocyte experiments. Given the published literature on hepatoprotective STAT5 inhibiting PPAR signaling (to prevent steatosis) and to activate cell cycle blocking genes (to prevent cancer) might se the molecular basis for our findings in *NIK*-deficient mice [37—40].

2.5. NIK inhibits GH-induced STAT5 activation via JAK2S633 phosphorylation

Our next aim was to examine the molecular mechanism by which *NIK* blunts STAT5 signaling. To evaluate the effect of hepatic *NIK* deficiency *ex vivo*, we stimulated primary hepatocytes with growth hormone (GH) to robuytly activate STAT5 signaling and with GH/TWEAK to determine the impact of NIK stabilization on STAT5 signaling (Figure 4A—B, Figure S5A). While *NIK*-deficient hepatocytes were more sensitive towards GH-induced STAT5 activation, they retained their GH sensitivity upon GH/TWEAK co-treatment. Consistently, GH/TWEAK stimulation drastically blunted STAT5 activation in control hepatocytes. Again, hepatocyte-specific *NIK* deficiency had only minor effects on IL-6 or IL-6/TWEAK-induced STAT3 as well as IFNγ or IFNγ/TWEAK-stimulated STAT1 activation (Figure S5B-E).

Although a recent report demonstrated NIK/IKK1-mediated JAK2/STAT3 inhibition in liver regeneration [25], how NIK interferes with STAT5 signaling has not yet been described. Therefore, we utilized MEFs that allow for HTNC-mediated expression of a stable Flag-tagged *NIKΔT3* construct to study NIK protein interactions upon GH stimulation using anti-Flag immunoprecipitation (Figure 4C). The *NIKΔT3* construct lacks the TRAF3 binding site (TRAF3 targets NIK for proteasomal degradation) [41]. Consistent with our previous experiments, GH stimulation revealed a blunted STAT5 activation in NIKΔT3-expressing MEFs (Figure S5F). Next, we used control and NIKΔT3-expressing MEFs in co-immunoprecipitation experiments where we pulled down NIKΔT3 via its Flag tag after 0 and 15 min of GH stimulation. While this experiment revealed no direct interaction between NIK and STAT5, NIKΔT3 immunoprecipitated with upstream JAK2 upon GH stimulation (Figure 4D). To evaluate whether hepatic NIK
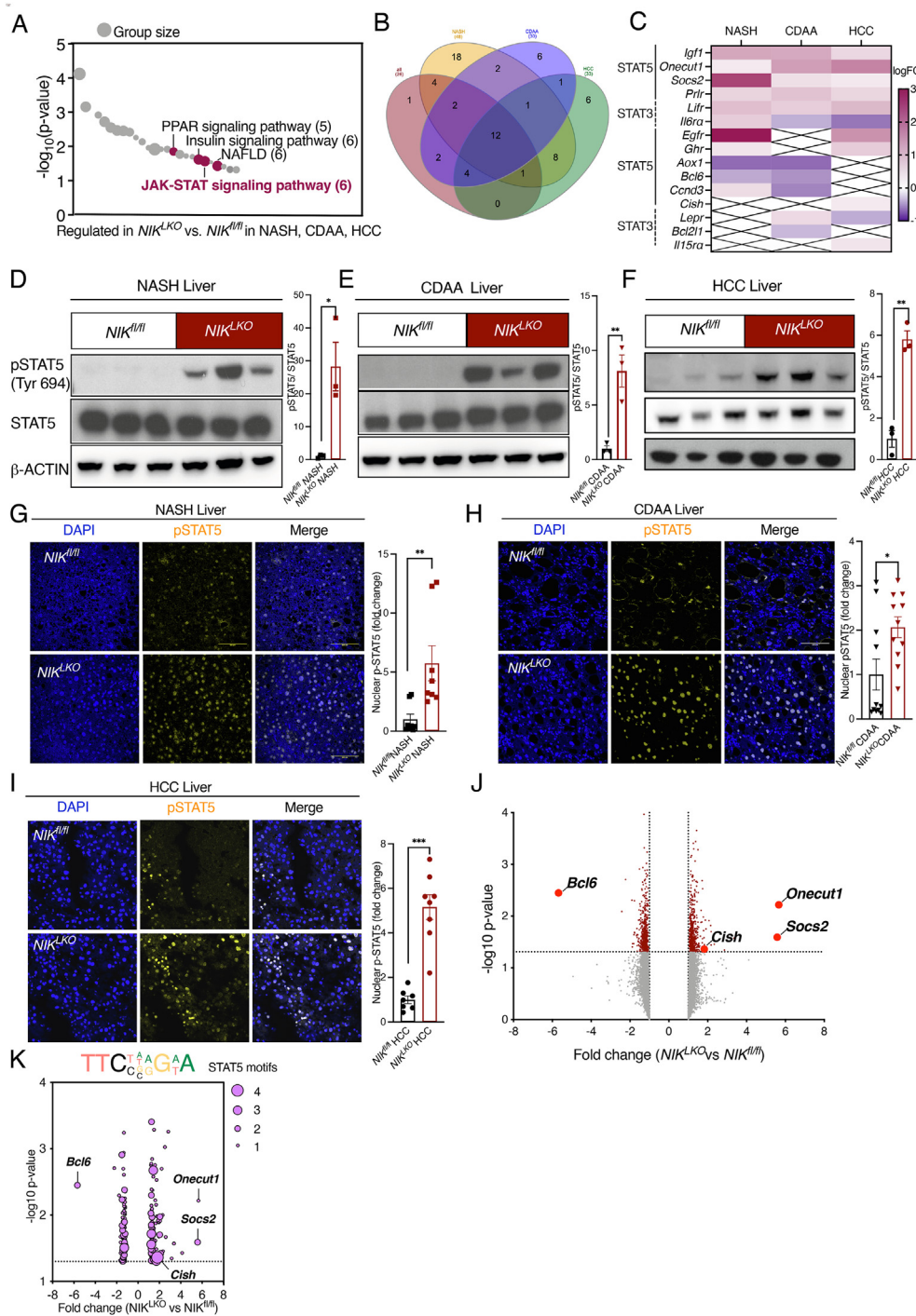
Figure 3: Hepatic NIK specifically blunts JAK2/STAT5 activation. A) Pooled GSEA analysis of *NIK^fl/fl* and *NIK^LKO* liver molecular signatures from the NASH, NASH to HCC transition and HCC study. Terms are sorted according to their P-value. Notable terms are highlighted; P-values are derived from Fisher's exact test and pass Benjamini-Hochberg corrected P < 0.05. B) Venn diagram of KEGG pathways obtained from the different models. C) Expression of JAK/STAT target genes defined by the JAK STAT gene set, GESA (systemic name M17411) in hepatocytes from the NASH, NASH to HCC transition and HCC study. Crossed out squares indicate the absence of a gene from the data set. D) Western blot analysis of pSTAT5, STAT5 and β-ACTIN levels in liver tissue from NASH-fed *NIK^fl/fl* and *NIK^LKO* mice (n = 3/3) and the respective quantification. E) Western blot analysis of pSTAT5, STAT5 and β-ACTIN levels in liver tissue from CDAA-fed *NIK^fl/fl* and *NIK^LKO* mice (n = 3/3) and the respective quantification. F) Western blot analysis of pSTAT5, STAT5 and β-ACTIN levels in non-tumor liver tissue from DEN-injected *NIK^fl/fl* and *NIK^LKO* mice (n = 3/3) and the respective quantification. G) Representative images of pSTAT5 staining (yellow) and DAPI (blue) in in liver tissue from NASH-fed *NIK^fl/fl* and *NIK^LKO* mice, scale bar 100 μm and respective quantification of pSTAT5 staining (n = 3/3). H) Representative images of pSTAT5 staining (yellow) and DAPI (blue) in in liver tissue from CDAA-fed *NIK^fl/fl* and *NIK^LKO* mice, scale bar 100 μm and respective quantification of pSTAT5 staining (n = 3/3). I) Representative images of pSTAT5 staining (yellow) and DAPI (blue) in in liver tissue from DEN-injected *NIK^fl/fl* and *NIK^LKO* mice, scale bar 100 μm and respective quantification of pSTAT5 staining (n = 3/3). J) Volcano plot of differential gene expression in liver tissue from DEN injected *NIK^fl/fl* and *NIK^LKO* mice (n = 3/3). Significantly regulated genes are shown in dark red. Genes selected for further analysis are shown in red. K) Motif search for STAT5 target genes on data sets from Affimetrix microarray (n = 3/3). Data are presented as mean ± SEM; *p ≤ 0.05, **p ≤ 0.01, versus control. Statistical analyses were performed using Student's *t*-test.
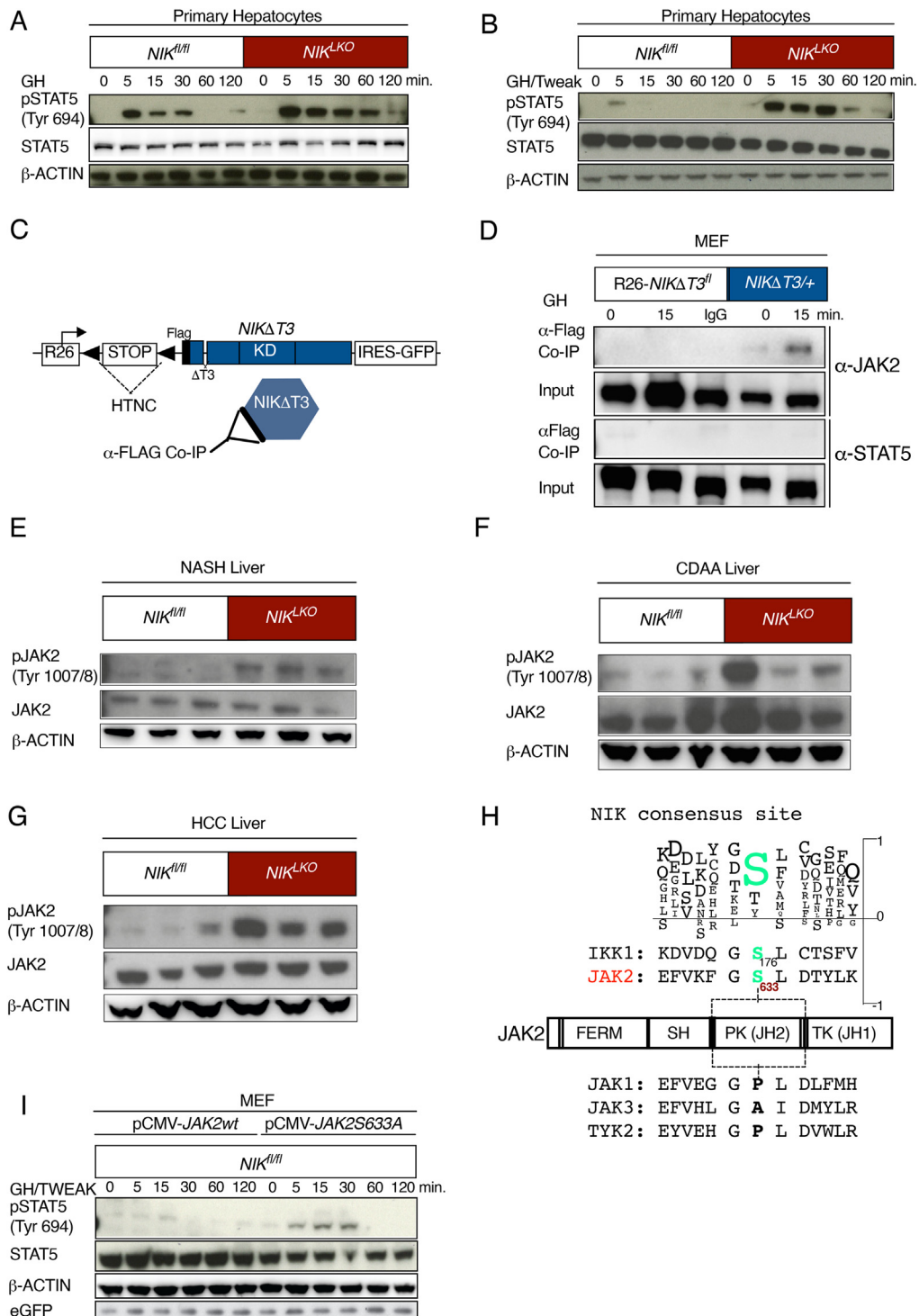
Figure 4: NIK inhibits GH-induced STAT5 activation via JAK2S633 phosphorylation. A) Western blot analysis of pSTAT5, STAT5 and β-ACTIN levels in primary hepatocytes isolated from *NIK^fl/fl* and *NIK^LKO* mice after *ex vivo* stimulation with GH. B) Western blot analysis of pSTAT5, STAT5 and β-ACTIN levels in primary hepatocytes isolated from *NIK^fl/fl* and *NIK^LKO* mice after *ex vivo* double stimulation with GH and TWEAK and the respective quantification (n = 3). C) *NIKTΔ3* construct used in *ex vivo* studies. After HTNC-mediated deletion of the loxP-flanked STOP cassette, *NIKTΔ3* is expressed under control of the ROSA26 promoter. D) For Co-IP R26-*NIKΔT3^fl* and NIKΔT3 MEFs were treated with GH for 0 min or 15 min. Cell extracts were co-immunoprecipitated (IP) with an α-Flag antibody and immunoblotted with JAK2 (n = 3) and STAT5. E) Western blot analysis of pJAK2, JAK2 and β-ACTIN levels in liver tissue NASH-fed *NIK^fl/fl* and *NIK^LKO* mice (n = 3/3). F) Western blot analysis of pJAK2, JAK2 and β-ACTIN levels in liver tissue from CDAA-fed *NIK^fl/fl* and *NIK^LKO* mice (n = 3/3) G) Western blot analysis of pJAK2, JAK2 and β-ACTIN levels in non-tumor liver tissue from DEN-injected *NIK^fl/fl* and *NIK^LKO* mice (n = 3/3). H) JAK2 domain structure (human). Positive regulatory phosphorylation sites are labeled green. Negative inhibitory phosphorylation sites are marked in red. FERM: FERM domain, PK: pseudokinase, TK: tyrosine kinase. Single letter amino acid sequence of NIK binding motif in IKK1 and the predicted binding motif in JAK2. Box indicates conserved amino acids. I) Western blot analysis of pSTAT5, STAT5 and β-ACTIN levels in *NIK^fl/fl* and *NIK^KO* MEF transfected with either pCMV-*JAK2wt* or with pCMV-*JAK2S633A* and treated with GH for the indicated timepoints (n = 3). Data are presented as mean ± SEM; *p ≤ 0.05, **p ≤ 0.01, versus control. Statistical analyses were performed using Student's *t*-test.

deficiency also enhances JAK2 activation in NASH, NASH to HCC transition and HCC, Western blot analyses of livers from the three mouse models were performed using anti-JAK2 P-tyrosine 1007/1008 antibody whose residues are essential for JAK2 activation [42]. Consistently, JAK2 activation was increased in *NIK*-deficient livers of all three mouse models (Figure 4E–G).

Thus, NIK inhibits activation of GH-induced STAT5 signaling by interfering with JAK2. Interestingly, when we compared the well described NIK phosphorylation motif in IKK1, namely serine 176 that lies within a conserved motif (GSLCTS), we identified a similar motif in the pseudokinase domain of JAK2 (GSLDTY) with serine 633 (S633) as a potential NIK phosphorylation site (Figure 4H). Of note, the nearby tyrosine 637 (Y637) is required for full activation of JAK2 upon leptin stimulation [43]. Despite high protein homology in the janus kinase (JAK) family, the other JAK molecules JAK1, JAK3 and TYK2 lack a serine residue at this site. Thus, we hypothesized that NIK phosphorylates JAK2 at S633 in an inhibitory manner to prevent JAK2 activation. To test this hypothesis, GH-induced STAT5 activation in control and *NIK*-deficient MEFs was examined upon transient transfection of a plasmid encoding a *JAK2S633A* mutant (pCMV-*JAK2S633A*). While we confirmed GH-induced STAT5 sensitivity in *NIK*-deficient MEFs in the presence of TWEAK, pCMV-*JAK2S633A* transfection rescued GH-induced STAT5 activation in TWEAK-treated control MEFs (Figure S5G-H). To exclude outcompetition of NIK action via overexpression of JAK2S633 A, we separately transfected pCMV-*JAK2wt* and pCMV-*JAK2S633A* into control MEFs and stimulated with GH and TWEAK (Figure 4I). Ultimately, this experiment revealed that pCMV-*JAK2wt* transfection failed to rescue MEFs from GH-induced STAT5 activation in the presence of TWEAK/stable NIK, whereas JAK2S633 A expression restored STAT5 activity even when NIK was stabilized.

Here, we identify a novel crosstalk between NIK and JAK2/STAT5 in progressive liver disease. Transfection experiments suggest that NIK-mediated S633 JAK2 phosphorylation inhibits activation of JAK2, resulting in blunted GH-induced STAT5 activation and its ability to prevent hepatoprotective gene expression.

2.6. NIK crosstalk with JAK2/STAT5 in human HCC

To address whether our finding in mice translates to human disease, we performed GH and GH/TWEAK stimulation experiments in human HCC-derived HepG2 cells, revealing blunted GH-induced STAT5 activation in the presence of TWEAK (Figure S6A-B). Assessment of NIK protein expression via immunohistochemistry of human HCC samples revealed NIK expression in all three tumor grades with the highest protein abundance in tumor grade 3 (Figure 5A). Consistently, we detected significantly elevated *NIK* (*Map3k14*) mRNA in a commercial cDNA array prepared from HCC (Grade 1–3) and normal human liver tissues (Figure 5B). These results indicate robust NIK expression at the mRNA and protein levels in human HCC. Evaluation of pSTAT5 showed significantly blunted STAT5 activation in HCC grade 3, with the highest NIK immunoreactivity (Figure 5C). Therefore, our data strongly argue for reciprocal crosstalk between NIK and inhibition of STAT5 in human HCC.

We also evaluated global gene expression of samples obtained from matched human non-tumor and tumor (HCC) biopsies. 3487 genes were differentially regulated between the groups that contributed to upregulation of DNA replication, cell cycle, and cancer promoting pathways in tumor tissue, whereas analysis of non-tumor tissue revealed mainly an enrichment of metabolic pathways such as fatty acid degradation, fatty acid metabolism, and PPAR signaling (Figure 5D–E). When we compared the differentially expressed human genes with the results from the mouse HCC microarray, an overlapping signature of 151 genes was observed (Figure 5F–G). Strikingly, 43.7% of the overlapping genes contained STAT5 binding motifs in their promoter including the *bona fide* STAT5 targets *SOCS2*, *ONECUT1*, *IGF1* and *CDKN2B*. We surmise that the inhibitory action of NIK on JAK2/STAT5 is indeed conserved between mice and humans. Lastly, overlap of non-canonical NFκB motifs between human and mouse gene expression identified only a minority of genes (Figure S6C).

Taken together, our mouse and human data identified a reciprocal crosstalk between NIK and JAK2 in the liver. NIK impairs STAT5 signaling via JAK2 inhibition. This newly identified mechanism promotes the development of NASH, NASH to HCC transition and HCC. Given the fundamental consequences of STAT5 action on the cell cycle and on lipogenic gene expression, our findings might be amenable for future therapeutic interventions in the treatment of NASH and HCC.

3. DISCUSSION

The worldwide rising obesity pandemic predisposes to fatal liver disorders such as NASH and malignant HCC transformation. The metabolic syndrome is a key feature for the sequential development of steatosis, steatohepatitis, hepatic fibrosis, and cirrhosis and ultimately to the increased frequency of HCC. However, the underlying pathways promoting progression from NASH to HCC are only poorly understood. Extensive data exist revealing impaired GH downstream signaling and low IGF1 expression in human NASH and HCC as a result of inflammation [44—48]. In fact, inflammation causes a state of hepatic growth hormone resistance via blunting JAK2 activation, however still to unknown mechanisms [49—51].

Our results unequivocally reveal *the* inhibitory action of *NIK* on JAK2/STAT5 signaling as a common prerequisite for chronic NASH and HCC experiments, but not in acute DEN and hepatocyte protocols. *NIK* deficiency was accompanied with improved STAT5 signaling that not only prevented hepatic lipid accumulation in NASH but also arrested the cell cycle to reduce liver cancer burden in NASH to HCC and HCC mouse models. STAT5 signaling decreases hepatic fat metabolism at least in part through regulation of fatty acid transporter CD36 [52] and a bidirectional inhibitory crosstalk between STAT5 and PPAR exists, that is able to reduce lipogenic PPAR target gene expression by approximately 80% [40]. Furthermore, hepatic *NIK* deficiency did not affect NFκB-regulated gene expression but instead affected classical STAT5 target genes previously reported to arrest cell cycle, prevent steatosis/NAFLD and HCC development [38,53]. Thus, our data reveal that hepatic *NIK* deficiency could be attributed to improved STAT5 signaling that verifies NIK as an inhibitor of STAT5 signaling. However, the inhibitory function of NIK did not directly affect STAT5 but instead via upstream JAK2 inhibition. JAK2 acts downstream of multiple cytokine and hormone receptors, but our data suggest NIK-mediated phosphorylation of JAK2 S633 to specifically impair STAT5 but not STAT3 nor STAT1 signaling. This specificity of NIK on JAK2/STAT5 axis might be explained by the restricted signaling capacity of the growth hormone receptor (GHR) that exclusively depends on JAK2 activity to activate STAT5 [54—56] but cannot use alternative JAK1, JAK3 and TYK2 molecules that do not contain the NIK phosphorylation motif. The largely unaffected STAT3 phosphorylation in the presence of NIK results from the fact that IL-6R signaling can utilize JAK1, JAK2 and TYK2 for STAT3 activation whereas STAT1 is activated by both JAK1 and JAK2 activity. Thus, the specific inhibitory action of NIK on GH-induced STAT5 might be a consequence of the critical dependence of the GHR on JAK2 activity that is the only JAK containing S633 in the predicted NIK motif.
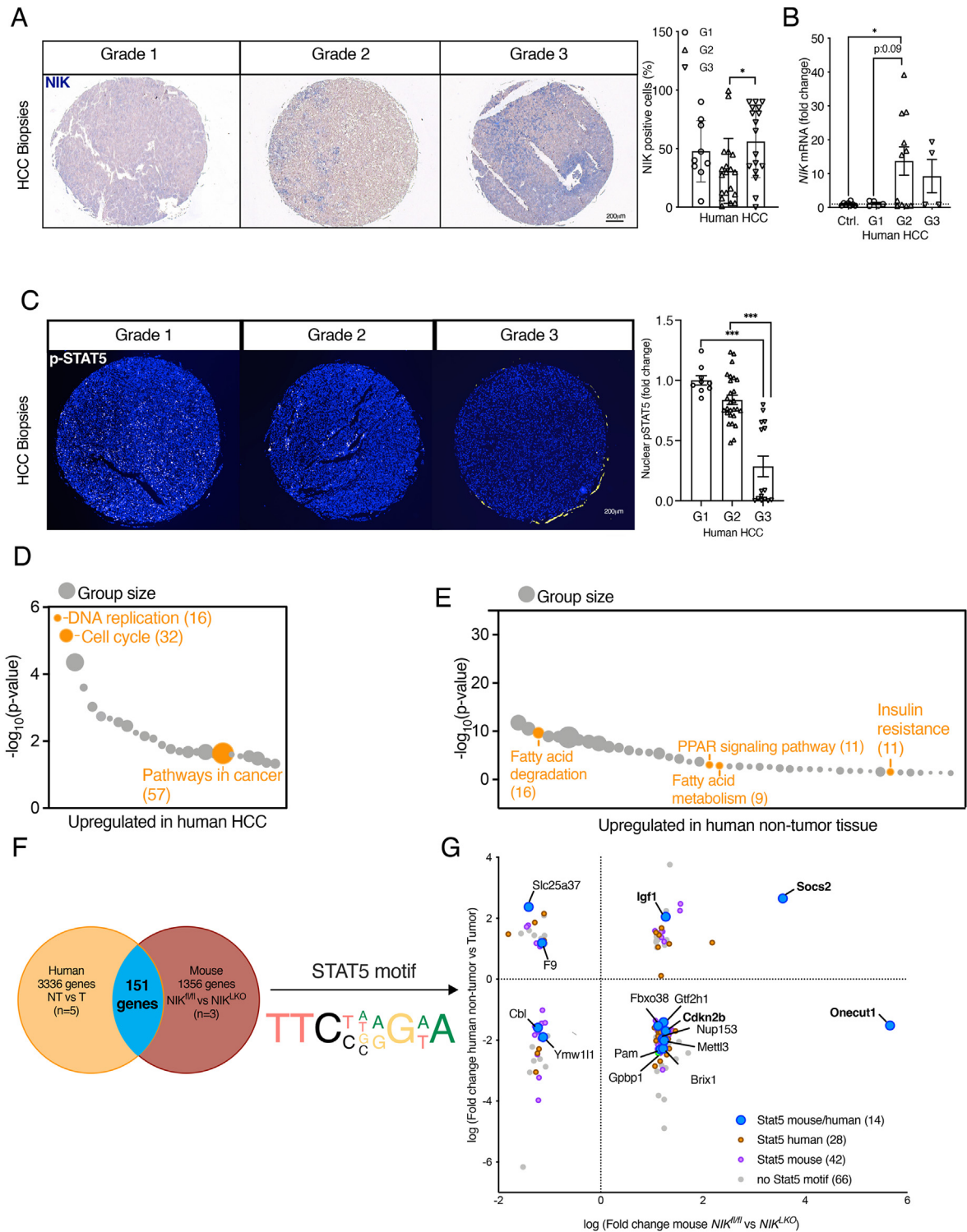
Figure 5: NIK crosstalk with JAK2/STAT5 in human HCC. A) qPCR analysis of human *NIK* mRNA expression in control tissue biopsies and human HCC biopsies. The biopsies are classified according to their tumor grade into Grade1 (well differentiated), Grade 2 (moderately differentiated), Grade 3 (poorly differentiated). Control: n = 8, Grade 1: n = 5; Grade2: n = 11; Grade 3: n = 4. B) Alkaline phosphatase staining of NIK in human HCC tissue biopsies, scale bar 200 μm. C) Representative images of pSTAT5 staining (yellow) and DAPI (blue) in human HCC tissue biopsies, scale bar 200 μm. GSEA analysis of human HCC non-tumor and human HCC tumor molecular signatures that are upregulated in human HCC. Notable terms are highlighted; P-values are derived from Fisher's exact test and pass Benjamini-Hochberg corrected P < 0.05. D) GSEA analysis of human HCC non-tumor and human HCC tumor molecular signatures that are upregulated in human non-tumor tissue. Notable terms are highlighted; P-values are derived from Fisher's exact test and pass Benjamini-Hochberg corrected P < 0.05. E) Overlap of human and mouse gene signature. Scatterplot of fold change $NIK^{fl/fl}$ vs NIK^{LKO} against human non-tumor vs tumor. All genes plotted are significant both in the human and mouse data set. Data are presented as mean ± SEM; *p ≤ 0.05, **p ≤ 0.01, versus control. Statistical analyses were performed using one-way Anova.

JAK2 S633 is located in a linker region between the N and C lobes of the JH2 pseudokinase domain that is critical for the conformational changes required to control kinase activity [57]. JAK2 mutants lacking the JH2 domain show uncontrolled activity [58] whereas a common JH2-intrinsic acquired JAK2 V617F mutation renders JAK2 constitutively active driving a group of myeloproliferative diseases [59—62]. While our experiments provide only indirect evidence of inhibitory JAK2 S633 phosphorylation, JAK2 serine/threonine phosphorylation *per se* and more specifically S523 phosphorylation negatively regulate JAK2 activity [63—65]. Moreover, a recent report discovered a context-dependent NIK/IKK1 inhibitory action on JAK2 to inhibit STAT3 in partial hepatectomy. Thus, in line with these data, our experiments suggest a new level of JAK2 regulation via inhibitory NIK-mediated S633 phosphorylation in the JH2 pseudokinase domain crucial to control JAK2 activity.

Our study also underlines the conservation of NIK impacting on JAK2/STAT5 axis between human and mouse. Expression of TWEAK and its receptor Fn14 are increased in human fatty liver diseases [66] and our data that NIK impairs JAK2/STAT5 activation in human HepG2 cells and HCC tissue as well as that most of regulated overlapping gene expression between mouse and human HCC is regulated by STAT5 signaling supports our findings. Consistently, a recent publication that integrated proteogenomic in HBV-related human HCC has revealed that deregulation of cell cycle control, oxidative phosphorylation, and fatty acid metabolism caused different outcomes on probability of survival. Here, altered STAT5 signaling has been identified among three different proteomic subgroups, thereby further supporting the translational aspect of our study to human disease [67].

Here, we define a novel conserved molecular link between hepatic NIK and JAK2/STAT5 signaling in NASH, NASH to HCC and HCC development. Therefore, hepatic NIK inhibition accompanied with STAT5 sensitization might be a potential strategy to treat NASH and prevent the progression from NASH to HCC.

CONTRIBUTIONS

DATA AVAILABILITY

Data will be made available on request.

ACKNOWLEDGEMENTS

CONFLICT OF INTEREST

The authors have declared no competing interests and no conflicts of interests exist.

APPENDIX A. SUPPLEMENTARY DATA

Supplementary data to this article can be found online at https://doi.org/10.1016/j.molmet.2022.101626.

METHODS

Contact for Reagent and Resource Sharing

Additional information and requests for resources or reagents used in this paper should be directed and will be fulfilled by the Lead Contact, F. Thomas Wunderlich (Thomas.Wunderlich@sf.mpg.de).

Animal Care

All animal procedures were conducted in compliance with protocols approved by local government authorities (Bezirksregierung Köln). Permission to maintain and breed mice was issued by the Department for Environment and Consumer Protection - Veterinary Section, Cologne, NRW, Germany (84-02.04.2014.A074 and 84-02.04.2019.A324). All animal procedures were performed in accordance with NIH guidelines. Mice were housed in individually ventilated cages (IVCs) at $22°C-24°C$ using a 12-hour light/dark cycle. Animals had access to water and food ad libitum. Food was only withdrawn if required for an experiment during defined fasting periods. If not stated otherwise all experiments have been performed in male mice.

Animal Diets

Mice had ad libitum access to either a normal chow-diet (R/M-H; Ssniff Diet) containing 57% of calories from carbohydrates, 34% calories from protein and 9% calories from fat, a control-diet (CD; EF D12450B; Ssniff Diet) containing 67% of calories from carbohydrates, 20% of calories from protein and 13% of calories from fat, a EF NASH diet (NASH; E15766-340; Ssniff Diet) containing 42% calories from carbohydrates, 18% of calories from protein and 40 % of calories from fat, a EF Control to NASH diet (CD to NASH diet; E15767-040; Ssniff Diet) containing 65% calories from carbohydrates, 22% of calories from protein and 13 % of calories from fat, a Choline free, lard,1 % cholesterol diet (CDAA diet; S2159-E042; Ssniff Diet) containing 58% calories from carbohydrates, 11% of calories from protein and 31% of calories from fat, or a control to choline free diet (CSAA diet; E15668-041; Ssniff Diet), containing 72% calories from carbohydrates, 12% of calories from protein and 16% of calories from fat.

NASH Feeding Experiments

For the NASH feeding experiments, male mice were weaned at p21. Upon weaning, mice were separated into 3-4 animals per cage and co-housed with their littermates. At 6 weeks of age male mice were switched from the NCD diet to respective experimental diets. To study the metabolic hallmarks of NASH, mice were either exposed to a NASH diet or a control diet. To assess the fibrotic effect of NASH, mice were exposed to a CDAA or CSAA diet.

Diethylnitrosamine-Induced HCC

At P15 male mice were injected *i.p* with 25 mg/kg BW diethylnitrosamine (DEN) (Sigma). Upon weaning, the mice were separated into 3-5 animals per cage and co-housed with their littermates until the end of the study at 32 weeks of age. Mice were fed a control diet (Ssniff E15748) for 30 weeks.

Mouse Lines

The NIK$^{fl/fl}$ mouse line was a gift from Ari Waisman and Nadine Hövelymeyer (Institute for Molecular Medicine, Mainz). Homozgyous NIK$^{fl/fl}$ were crossed with Alfp-cre mice to generate a hepatocyte specific NIK knockout mouse. To verify the expression of the Alfp-Cre-recombinase and to detect the loxP flanked exons, each mouse was genotyped. Tail biopsies were taken after weaning of the mice. The biopsies were lysed in 500 μL tail lysis buffer (5mM EDTA pH 8.0; 0.2% SDS, 200 mM NaCl,

1x Proteinkinase K (Roche)) at 56 °C for at least 3 hours. Isolated DNA was precipitated by addition of 500 μL 2-propanol and pelleted by centrifugation (13,000 rpm, 15 minutes at RT). Supernatant was discarded and DNA was washed one time with 300 μL 70% ethanol. DNA was pelleted by centrifugation (13,000 rpm, 15 minutes at RT) and supernatant was discarded. DNA pellets were dried to allow complete evaporation of remaining ethanol and afterwards resuspended in 50 μL TE/RNAse A buffer. For genotyping of isolated DNA, Cre-specific (Alfp-Cre (senseTCCAGATGGCAAACATACGC, Alfp-Cre antisense GTGTACGGTCAGTAAATTGGAC) and NIK floxed- specific primer (NIK sense: TATGAACTGCTCCCGTTTCG, NIK antisense CCTGTGCATCACAGAGTA-TACTAGC) were used. For each sample 2 μL DNA were mixed with 22.8 μL of PCR-mastermix and 0.2 μL DreamTaq (Fermentas). PCR was performed by using primer-specific PCR-programs. Resulting gene fragments were analyzed by agarose gel electrophoresis using 2% agarose (Sigma) gels.

Metabolic Characterization

Insulin Tolerance Test

Insulin tolerance tests (ITTs) were performed in random fed mice. Food was removed and bedding was renewed prior to starting the experiment. Blood glucose concentrations were measured from whole venous blood using an automatic glucose monitor (Contour Ascensia, Bayer HealthCare, Germany). Following determination of body weights and basal blood glucose concentrations, mice received an intraperitoneal injection of 0.75 U/kg body weight or 0.375 U/kg body weight of human insulin (Insuman® Rapid, Sanofi Aventis) and blood glucose concentrations were measured again at 15, 30, and 60 min post injection. Food was withdrawn over the whole course of the experiment.

Glucose Tolerance Test

Glucose tolerance tests (GTTs) were performed in mice that had been fasted for 6 hours. Following determination of body weights and basal blood glucose concentrations, mice received an intraperitoneal injection of 20% glucose (10 mL/kg body weight; beta-pharm) and blood glucose levels were measured again at 15, 30, 60, and, 120 min post injection. Blood samples for glucose measurement were collected from the tail vein. Glycemia was assessed using a glucometer (Contour, Bayer).

Analysis of Body Composition

Body composition was analysed using micro-computed tomography (micro-CT)-based imaging of isoflurane-anesthetized mice. Data acquisition was performed in an IVIS Spectrum CT-scanner (Calpier LifeScience, USA) using the IVIS LivingImage Software V4.3.1. Quantification of fat mass was determined with a modification of the Vinci software package 4.61.0 ADDIN EN.CITE [69].

Organ Dissection and Tumor Scoring

Liver and white adipose tissue were extracted and weighed. Left and right medial lobes were embedded in tissue freezing medium (Leica) for subsequent histological analysis. The left lateral lobe was stored in 4% formalin for further pathological analysis. Tumors were quantified macroscopically by visual inspection. Therefore, livers were washed with ice-cold PBS and tumor numbers were counted and classified into small tumors (< 2mm) or large tumors (> 2 mm). For collection of tumor tissue samples, tumors of different sizes were extracted from the liver. All tissue samples were snap-frozen in liquid nitrogen and stored at -80 °C.

Aspartate Transaminase /Alanin Transferase Determination

Aspartate transaminase (AST) and Alanin transferase (ALT) activity in the serum as well as triglycerides and cholesterol were determined at the Institute of Clinical Chemistry of the University Hospital Cologne using standard techniques.

ELISA

IL-6 and TNFα ELISA

For the detection of hepatic IL-6 and TNFα levels commercially available pre-coated sandwich ELISAs (both R&D systems #MTA00B, #M6000B) were used. For the IL-6 ELISA, a linear standard curve was prepared ranging from 500 pg/mL to 7.8 pg/mL mouse IL-6 (R&D systems). For TNFα ELISA, a standard curve was prepared ranging from 700 pg/mL to 10.9 pg/mL. 25 μL IL6-Assay Diluent (R&D systems) or TNFα-Assay Diluent (R&D systems) were added to microplate wells.

25 μL standard or 25 μL protein sample (50 mg of liver lysate diluted in NP40 buffer), respectively, were added and incubated for 2 hours at RT. Wells were washed four times using 400 μL wash buffer (R&D systems). 50 μL mouse IL-6 conjugate (R&D systems) or TNFα conjugate (R&D systems) were added and incubated for 2 hours at RT. Wells were washed again four times using 400 μL wash buffer. Subsequently, 100 μL substrate solution (R&D systems) were added and incubated for 30 minutes protected from light at RT. 100 μL stop solution (R&D systems) were added to inactivate enzymatic reaction and absorbance was measured at 450 nm with wavelength correction of 570 nm using a plate reader.

LIGHT ELISA

For the detection of hepatic LIGHT levels commercially available ELISA kits (R&D systems #DY1794) were used. A linear standard curve was prepared ranging from 16000 pg/mL to 250 pg/mL using recombinant mouse Tweak standard (R&D systems). To prepare the plate, the capture antibody was diluted according to manufacturer's instructions and a 96-well plate was coated, blocked and prepared for sample addition according to manufacturer's instructions. 100 μL standard or 100 μL protein sample (50 μg of liver lysate diluted in NP40 buffer), respectively, were added and incubated for 2 hours at RT. Wells were washed three times using 400 μL wash buffer (R&D systems). 100 μL mouse detection antibody (R&D systems) were added and incubated for 2 hours at RT. Wells were washed again three times using 400 μL wash buffer. Subsequently, 100 μL Streptavidin-HRP (R&D systems) were added and incubated for 20 minutes protected from light at RT. Subsequently, 100 μL substrate solution (R&D systems) were added and incubated for 20 minutes protected from light at RT. 50 μL stop solution (R&D systems) were added to inactivate enzymatic reaction and absorbance was measured at 450 nm with wavelength correction of 570 nm using a plate reader

Tweak ELISA

For the detection of hepatic TWEAK levels commercially available ELISA kits (R&D systems #DY1237) were used. A linear standard curve was prepared ranging from 1000 pg/mL to 15.6 pg/mL using recombinant mouse TWEAK standard (R&D systems). To prepare the plate, the capture antibody was diluted according to manufacturer's instructions and a 96-well plate was coated, blocked and prepared for sample addition according to manufacturer's instructions. 100 μL standard or 100 μL protein sample (50 μg of liver lysate diluted in NP40 buffer), respectively, were added and incubated for 2 hours at RT. Wells were washed three times using 400 μL wash buffer (R&D systems). 100 μL mouse detection antibody (R&D systems) were added and incubated for 2 hours at RT. Wells were washed again three times using 400 μL wash buffer. Subsequently, 100 μL Streptavidin-HRP (R&D systems) were added and incubated for 20 minutes protected from light at RT. Subsequently, 100 μL substrate solution (R&D systems) were added and incubated for 30 minutes protected from light at R50 μL stop solution (R&D systems) were added to inactivate enzymatic reaction and absorbance was measured at 450 nm with wavelength correction of 570 nm using a plate reader.

Caspase3 activity assay

Caspase 3 activity was determined by measuring cleaved caspase 3 in liver lysates using PathScanCleaved Caspase 3 ELISA kit (Cell Signalling #7190) according to manufacturer's instructions.

Insulin Elisa

Mouse serum insulin concentrations were determined using the Ultra Sensitive Mouse Insulin ELISA Kit (Crystal Chem, Cat #90080) according to the manufacturer's instructions. 5 μL of serum samples from random fed mice or 5 μL of working mouse insulin standards were mixed with 95 μL of sample diluent in wells of a 96-well microplate coated with guinea pig anti-insulin antibody and incubated for 2 hr at 4°C. Afterward unbound material was removed in 5 consecutive washing steps using 300 μL washing buffer per well and step. Subsequently, horseradish peroxidase-conjugated anti-insulin antibody was bound to the anti-insulin antibody/mouse insulin complexes immobilized to the microplate well by adding 100 μL of anti-insulin enzyme conjugate followed by incubation for 30 min at room temperature. Excess conjugate was removed in 7 consecutive washing steps using 300 μL wash buffer per well and step. Bound conjugate in the microplate was detected by the addition of 100 μL of 3, 3′, 5, 5′-tetramethylbenzidine substrate solution and incubation for 40 min at room temperature in the dark. Reactions were stopped with 100 μL of stop solution per well and optical density of each well was determined using a FilterMax

F5 Multi-Mode microplate reader and SoftMax Pro 6.3 software (Molecular Devices). Readings at 630 nm were subtracted from readings at 450 nm to correct for optical imperfections in the plate. For quantification a four parameter curve-fit standard curve (range: 0.1-12.8 ng/mL) was used and insulin concentrations of samples were calculated accordingly.

Cell Culture Experiments

Primary Hepatocytes

To isolate primary hepatocytes, mice were sacrificed by cervical dislocation and the abdomen was opened longitudinally. A 26G cannula was inserted into the vena cava and fixated. The hepatic portal vein was cut and liver was perfused for 5 minutes with pre-warmed hepatocyte solution I (0.5 M EGTA, EBSS w/o Mg2+ and Ca2) to remove residual blood from the liver. Afterwards, livers were perfused for 5 minutes with 50 mL pre-warmed hepatocyte solution III (10 mM HEPES, EBSS with Mg2+ and Ca2, collagenase IV). Perfused livers were extracted, the gall bladder was removed and the remaining tissue was transferred into 10 mL cold hepatocyte solution II (10 mM HEPES, EBSS with Mg2+ and Ca2). Isolated cells were filtered through a 70 μm cell strainer, collected in 50 mL falcon and pelleted by centrifugation (1,200 rpm, 5 minutes at 4°C). Cells were washed with 10 mL cold hepatocyte solution II followed by one wash with 10 mL cold hepatocyte cultivation medium. 2.5 x 10^5 to 5 x 10^5 hepatocytes were seeded onto collage-coated 6-well plates in hepatocyte cultivation medium. Medium was changed after 4 hours of plating the cells. For stimulation of primary hepatocytes with growth hormone (GH) (Biomol, #97074) and Tweak (R&D, #1237-TW-025/CF), the cultivation medium was replaced with hepatocyte starvation medium (2%FCS) after 4 hours of cultivation. Hepatocytes were starved overnight. For STAT5 inhibition experiments, hepatocyte media were replaced with 200μM STAT5 inhibitor for 9h in 2% FCS containing media. Subsequently, mRNA isolation and qPCR was done as described. For Western blot, hepatocytes were stimulated with 500 ng/mL growth hormone or 90 ng/mL Tweak or double stimulated with 500 ng/mL growth hormone and 90ng/mL Tweak. Hepatocytes were treated for 0, 5, 15, 30, 60, and 120 minutes at 37 °C.

HepG2 Cells

HepG2 cells were purchased from ATCC (ATCC HB-8065) and cultured in DMEM medium (Gibco) containing 10% FBS with 5% CO_2 at 37C°C. Prior to stimulation, HepG2 cells were cultured in starvation medium (2% FCS). HepG2 cells were stimulated with 500 ng/mL growth hormone (PeproTech, #100-40) or 90 ng/mL Tweak (R&D, #1090-TW) or stimulated with 500 ng/mL growth hormone and 90ng/mL Tweak for 0, 5, 15, 30, 60, and 120 minutes at 37 °C.

Mouse Embryonic Fibroblasts

Mouse embryonic fibroblasts (MEFs) were isolated from E13.5 embryos. Pregnant females were sacrificed by cervical dislocation, the uterus was removed and placed in PBS (Gibco). Under sterile conditions the uterus was opened and embryos were collected. Chorion and amnion of each embryo was removed and embryos were washed in cold PBS. Fetal livers were removed and heads were taken for DNA isolation and subsequent genotyping. Embryonic tissue was dissociated in 1 mL 2.5% trypsin (Gibco) and incubated for 15 minutes at 37 °C. Digestion was quenched by addition of equal amounts of MEF-medium (DMEM high glucose GlutaMax, 1% Sodium Pyruvate, 1% L-Glutamine, MEM-NEAA, 12% FCS). Embryonic tissue was passed through a 100 μm strainer into a 50 mL falcon and pelleted by centrifugation (300 g, 5 minutes at RT). Pelleted cells were suspended and cultivated on an appropriate number of cell culture dishes. Medium was changed after 2 days and cells were further cultivated until they reached confluence. MEFs were SV40 immortalized via transfection of a SV40-expressing plasmid. If not stated otherwise, primary MEFs were used.

Transfection of Mouse Embryonic Fibroblasts with pCMV-Jak2wt or pCMV-Jak2-S633A

For transfection with GeneJuice (Novagen), MEFs were seeded in 6 well plates at a density of 2.0x 10^5cells/well. According to manufacturer's instructions, cells were grown overnight to reach 80-90% confluency before transfection. 3 μL of GeneJuice reagent were added to 100 μL of Optimem (Gibco), mixed and incubated for 5 minutes at RT. 1.5 μg pCMV-Jak2-wt or pCMV-Jak2-S633A and 0.5 μg pCMV EGFP reporter plasmid were added into the GeneJuice mixture and incubated at RT for 15 min. The mixture was added dropwise to cells grown in 3 mL complete medium without antibiotics. The transfection procedure was repeated on the following day.

In order to generate NIK knockout MEFs transfected with either pCMV-Jak2-wt or pCMV-Jak2-S633A, the cells were treated with HTNC-Cre. Therefore, MEFs were treated with 5 μM HTN-Cre in PBS:DMEM (1:1) for 16 hours. MEFs treated with only PBS: DMEM served as wildtype control cells. After 16 hours, medium was changed to complete MEF medium and cells were grown for 24 hours. For time course experiments, MEFs were starved in 2% FCS complete medium overnight and were stimulated on the following day with 500 ng/mL growth hormone or 90 ng/mL Tweak or stimulated with 500 ng/mL growth hormone and 90 ng/mL Tweak. MEFs were treated for 0, 5, 15, 30, 60, and 120 minutes at 37 °C.

Analysis of Gene Expression

Isolated hepatocytes were first homogenised using the QIAshredder kit (#79654, Qiagen), and total RNA was isolated using an RNeasy Kit (#74106, Qiagen). RNA was reverse transcribed using the High Capacity cDNA Reverse Transcription Kit (#4368813, Applied Biosystem). 100 ng cDNA was used for quantitative determination of gene expression levels using TaqMan Gene Expression Master Mix (4369542, Applied Biosystems) together with TaqMan probes (Applied Biosystem).

Human Commercial cDNA Array

NIK mRNA levels were analyzed in a commercial cDNA array (origene, #LVRT101) prepared from hepatocarcinoma (Grade 1-3) and healthy human liver tissues.

Microarray Analysis of Murine Liver Samples

Liver tissues were lysed using Trizol (QIAGEN), and RNA was extracted via phenol-chloroform extraction; 500 μL Trizol was added to tissue samples and homogenised using FastPrep (MP Biomedicals). To clear the supernatant from cell debris, samples were centrifuged (13,000 rpm for 15 min at 4 °C), and supernatants were transferred into new tubes. Samples were incubated for 5 min to allow proper dissociation of nucleotide complexes. By adding 100 μL chloroform (Sigma) and centrifugation (13,000 rpm for 15 min at 4 °C) a phase separation was achieved with RNA concentrated in the upper aqueous phase. The aqueous phase was transferred into new tubes and mixed with equal volume of 70% ethanol. Whole sample volume and any precipitates were loaded onto RNeasy spin columns (QIAGEN), and RNA isolation was continued according to the RNeasy Mini Kit protocol, including on-column DNA digestion (both QIAGEN). RNA integrity was determined using an Agilent Bioanalyzer (Agilent). RNAs with a RIN $\geq$ 9 and a concentration higher than 100 ng/μL without protein contaminations were used for microarray analysis and hybridised to GeneChipMouse Gene 2.0 ST Arrays (Affymetrix) according to the manufacturer's instructions. Affymetrix Powertoolsand the robust multiarray average method were used for background correction, quantile normalisation, and summarisation of the raw intensity values. R software (Version 2.13.1) along with the Bioconductor software package were used for the robust multiarray average method, statistical analysis (two-sided Student's t test), calculation of the change in intensity and illustrations. Genes were considered significantly deregulated with a P value of $\leq$0.05 and a fold change of $\geq$1.2.

Motif search

Motif detection was carried out using the R language version 3.4. We attached the information ensembltranscript id, ensembl transcript name, ensembl gene id and ensembl gene name to the microarray probesetIDs (affy_mogene_2_1_st_v1) using Biomart 59. Next, we determined the significant genes using a p-value cutoff of 0.05 and a minimum log-fold-change of 1.2. For all significant genes we extacted the genomic sequence of the 2000 BP upstream transcript flanc. We then proceeded querying the transcript flanc for the motifs TTCC[CTA][GA][GT][AC]A (Stat1) and TTC[TC][ATGC][AG]G[AT]A (Stat5A/B).

Human Liver Samples

Tissue samples from the tumor and from surrounding nontumorous liver tissue from 5 patients (3 male/ 2 female) with HCC were used for this study. HCC was diagnosed preoperatively by computed tomography or magnetic resonance imaging. All patients were treated surgically and received the same postoperative care in the Department of Surgery, Campus Virchow Klinikum at the Charité — Universitätsmedizin Berlin. The diagnosis was confirmed postoperatively by a pathologist. As well, the

surrounding tumor free tissue was evaluated by the pathologist. The study was approved by the local ethics committee (Ethikommission der Charité Berlin, Germany, Approval Number EA4/080/14), and patients gave their written informed consent to participate in the study.

Microarray Analysis Human Liver Samples

RNA was isolated from tumor and tumor-free liver samples of 5 patients using Trizol Reagent (Invitrogen, Carlsbad, CA) following the manufacturer's instructions and further purified using RNeasy mini columns (Qiagen). RNA was then hybridized to Human6 Expression v3 and v4 beadchips (Illumina, San Diego, CA) following protocols listed on the Gene Expression and Genomics Unit of the NIA (http://www.grc.nia.nih.gov/branches/rrb/dna/index/protocols.htm). Raw data were subjected to Z normalization. The Z ratio (between non-tumor (NT) and tumor (T) tissues, defined as treatment A and B, respectively) is given by z(A)-z(B)/std dev. Individual genes with Z ratio > 1.5, p value < 0.05, and avg intensity > 0 were considered significantly changed. For parametric analysis of gene set enrichment (PAGE), a list of pathways was obtained from http://www.broad.mit.edu/gsea/msigdb/msigdb_index.html (C2 collection). Our expression data was tested for gene set enrichment using the PAGE method as previously described. For each Z (pathway) a p value was also computed in JMP 6.0 to test for the significance of the Z score obtained. These tools are part of DIANE 6.0 and are available at http://www.grc.nia.nih.gov/branches/rrb/dna/diane_software.pdf.

Gene expression data was deposited in NCBI Gene Expression Omnibus (http://www.ncbi.nlm.nih.gov/geo/) under the accession number

GSE146049

Single Nuclei Isolation for Single Nuclei Sequencing

For single nuclei isolation 120 mg of liver were homogenized using a glass dounce tissue grinder in 2 mL of ice-cold EZ Prep buffer (Sigma, cat#Nuci-101) and incubated on ice for 5 min, with additional 2 mL of ice-cold EZ Prep buffer. Nuclei were centrifuged at 500 x g for 5 min at 4C°, the supernatant was removed, nuclei were washed with 4 mL ice-cold EZ Prep buffer and incubated on ice for 5 minutes. This step was repeated once more. After the second centrifugation step, nuclei were washed in 4 mL Nuclei suspension buffer (1x PBS, 0.01% BSA, 0.1% RNase inhibitor (Clontech Cat#2313A)). Isolated nuclei were resuspened in 2 mL NSB, filtered through a 30 μm cell strainer.

The nuclei suspension was stained with DAPI (1:1000, 62248, Thermo Fisher Scientific) as a nuclear marker. Cell sorting was performed using a BD FACSAriaIllu with FACSDiva 8.0.1 software. Single nuclei were sorted at 4°C using a 70 μm nozzle and sheath pressure was set at 70 psi. 0.9 % NaCl was used as sheath fluid. Single nuclei were gated based on DAPI fluorescence. DAPI was excited by a 405 nm laser and the emission signal was detected using a 450/50 nm bandpass filter. Sorted DAPI positive nuclei were collected into 1xPBS buffer with 0.04% BSA for 10x genomics single cell sequencing.

cDNA was prepared according to the 10x Genomics Chromium Single Cell 3' Reagent Kit User Guide (v3.1 Chemistry) with the input of ∼16.000 nuclei in suspensions / sample. At this point, all cDNA fragments carried the 16nt cellular barcode and 12nt UMI at the Poly (dT) end. 25% (10 μL) of this cDNA solution continued with the original 10x Genomics protocol to create an Illumina 3mRNA library with P5 and P7 Illumina adapters. Sequencing was done on Illumina NovaSeq6000 systems finally leading to an estimated number of 8.483- 10.553 nuclei/sample. Cell ranger analysis (10x genomics) was done using the 4.0.0 pipeline version for Loupe Browser 4.1.0 evaluation of the data. The merged UMI matrix of all 6 samples was analyzed with Seurat v3.0 https://doi.org/10.1016/j.cell.2019.05.031). Cells were filtered to contain at least 800 UMIs, a maximum of 40000 UMIs and maximum mitochondrial proportion of 3%. We applied default Seurat pipeline parameters for most processing steps (https://satijalab.org/seurat/articles/pbmc3k_tutorial.html), using 2000 highly variable features and 30 principal components for graph construction and umap calculation. *Sctransform* was used to normalize each sample, followed by *FindIntegrationAnchors* and *IntegrateData* to build an integrated dataset across all diets and conditions for shared visualization and annotation (https://satijalab.org/seurat/v3.0/integration.html). Clusters were obtained with *FindClusters* at resolution=1.2 (after

iterating over multiple resolutions) on the integrated dataset. Clusters were assigned to major liver celltypes based on markers from: (SOURCE).). We manually grouped hepatocyte clusters into a second clustering level based on known markers ADDIN EN.CITE [70]. Cluster markers were detected with *FindMarkers*(wilcox-test). To compare samples within each diet, we split the data but retained the cluster-annotations and umap-coordinates. Comparisons between genetic conditions were calculated with *FindMarkers* to obtain a foldchange.

Immunoblot Analysis and Quantification

For protein isolation, liver tissue and hepatocytes were resuspended in cell lysis RIPA buffer (50 mM Tris-HCL, pH 7.5, 150 mM NaCl, 1 mM EDTA, 0.1% Natrium-Deoxycholate and phospho-inhibitor cocktail (Roche)) using a homogenizer (IKA) and incubated for 60 min at 4 °C (IKA Vibrax VXR basic) with intensive vortexing every 15 min. Supernatant was cleared via centrifugation (13,000 rpm for 15 min at 4 °C). For protein isolation from whole tissue, samples were homogenised in RIPA buffer (50 mM Tris-HCL, pH 7.5, 150 mM NaCl, 1 mM EDTA, 0.1% Natrium-Deoxycholate and phosphor-inhibitor cocktail (Roche)) using a FastPrep machine (MP Bio) and cleared via centrifugation (13,000 rpm for 15 min at 4 °C). Protein concentration was determined with a BCA Protein Assay Kit (Pierce™) according to manufacturer instructions. Samples were diluted to a final concentration of 10 mg/mL using Laemmli-sample buffer (BioRad). Protein denaturation prior to gel electrophoresis was performed by boiling the samples for 5 minutes at 95°C. Precasted polyacrylamide NuPAGE™ 4-12% Bis-Tris Protein Gels (Invitrogen™) were placed in a XCell SureLock™ Mini-Cell (Invitrogen™) filled with 1x NuPAGE® MOPS SDS Running Buffer (20X). Protein samples were loaded and separated by applying an electric field (200V). Proteins were blotted by using the Trans-Blot Turbo Transfer System. Membranes were blocked for 1 h at room temperature and probed with primary antibodies according to the manufacturer's instructions. After incubation, residual primary antibody was removed by washing three times for 10 min in TBS-T (50 mM Tris, 140 mM NaCl and 0.1% Tween20) and incubated for 1 hour with secondary antibody. After removal of residual secondary antibody, blots were incubated for 1 min in ECL substrate (#34076, ThermoFisher), imaged using developer machine (Agfa Curix 60) and quantified using ImageJ software. For regeneration, membranes were incubated in stripping buffer (62.5 mM Tris, pH 6.8, 2% SDS and 0.07% β-mercaptoethanol) for 20 min at 56 °C with mild agitation. Afterwards, stripped membranes were washed twice for 15 min in TBS-T. Blocking and antibody probing was performed as described above.

Co-Immunoprecipitation

To identify the binding target of NIK co-immunoprecipitation was performed. Therefore, a Dynabead Co-Immunoprecipitation kit (Novex) was used. First, 30 μg anti-Flag antibody (origene, #TA50011-100) were coupled to 1.5 mg Dynabeads and incubated on a roller at 37°C overnight. The bead-antibody mix was washed according to manufacturer instructions and stored at 4°C in SB buffer at a final concentration of 10 mg/mL. The Co-IP was performed using NIK T3 cells. NIK T3 cells were cultured on 10 cm dishes to 90% confluency and treated with recombinant HTN-Cre (5 μM) or PBS in PBS: DMEM (1:1) overnight for 18 hours. HTN-Cre treatment removed the STOP cassette and induced NIK overexpression. Cells, without HTN-Cre treatment served as wildtype control samples. On the next day, the medium was removed and replaced with conventional DMEM medium. To induce JAK2/STAT5 signalling axis, cells were treated with 500 ng/mL GH for 15 minutes. Subsequently, cells were harvested in PBS, centrifuged at 500 x g for 5 minutes at 4°C and the supernatant was removed. The cell pellet weight was determined and afterwards, the cell pellet was suspended in 1:9 ratio of cell mass to extraction buffer (Novex) and incubated on ice for 15 minutes. Subsequently, cells were centrifuged at 2,600 x g for 5 minutes at 4°C, the supernatant was transferred to a fresh tube and the protein concentration was determined by Nanodrop. For further co-immuno-precipitation 0.3 mg protein of samples and control samples were used. The Dynabeads-antibody mix was washed with 900 μL of extraction buffer (1 x IP buffer, 100 mM NaCl, 2 mM MgCl2,1 mM DTT, 100 mM PMSF), placed on a magnetic rack and the supernatant was removed. Washed Dynabeads were

incubated 0.3 mg of prepared cell lysate for 1 hour at 4°C. The Dynabeads Co-IP complex was washed with 200 μL extraction buffer by pipetting for a total of three times. To wash the beads, the Dynabeads Co-IP complex tube was placed on a magnet for 1 minute and the cleared supernatant was removed by pipetting. Subsequently, the Dynabeads Co-IP complex were washed with 1X LWB buffer (Novex), re-suspended in 60 μl EB buffer (Novex) and incubated on a roller for 5 minutes at RT. Tubes were placed on a magnet and the supernatant containing the purified protein complex was transferred to a clean tube and analyzed by Immunoblotting as above.

JAK2 Immunoprecipitation

The IP was performed using NIKDT3^{fl}, NIKDT3/+ and NIK^{KO} cells transfected with pCMV-Jak2-wt. For transfection with GeneJuice (Novagen), NIK and NIKDT3^{fl} MEFs were seeded in 10 cm plates at a density of 18x 10^{5}cells/well. According to manufacturer's instructions, cells were grown overnight to reach 70% confluency before transfection. 15 μL of GeneJuice reagent was added to 500 μL of Optimem (Gibco), mixed by vortexing and incubated for 5 min. at RT. Then 5 μg pCMV-Jak2-wt was added into the GeneJuice mixture and incubated at RT for 15 min. The mixture was added dropwise to cells grown in 10 mL complete medium without antibiotics. The transfection procedure was repeated on the following day.

In order to generate NIK knockout and NIKDT3/+ MEFs transfected cells were treated with 5 μM HTN-Cre in PBS:DMEM (1:1) for 16 hours. NIKDT3^{fl} treated with only PBS:DMEM served as wildtype control cells. After 16 hours, medium was changed to complete MEF medium and cells were grown for 24 hours. Cells were starved for 12 hours in 2% FCS starving medium and treated with 500 ng/mL GH for 15 minutes. Subsequently, cells were washed with ice-cold PBS and were harvested in RIPA Buffer. Next, proteins were isolated by placing cell lysates on ice for 15 minutes and vortexing of the samples. Crude protein lysates were collected as input. Cells were centrifuged at 14000 x g for 15 minutes at 4°C and the supernatant was collected. Protein concentration was determined by BCA protein assay kit (Pierce) and 2 mg of protein lysates were incubated with Jak2 sepharose bead conjugate (1:20) (#4089 Cell Signalling) or IgG isotype control sepharose beads and incubated overnight with rotation overnight at 4C°. Cells were microcentrifuged for 30 seconds at 4°C and the pellet was washed 5 times with RIPA Buffer. Supernatant was removed and 30 μL Laemmli Buffer was added and samples were heated at 70 C° for 10 min. Beads were removed by centrifugation.

Immunohistochemistry

Human liver samples

NIK Alkaline- phosphatase staining on human HCC liver stances

To evaluate NIK protein expression in human HCC samples, a liver carcinoma tissue array (Biomax.us, BC03013) was stained for NIK (Cell Signaling, #4994). The array was dehydrated at 60°C for 30 minutes, deparaffinized and heat-mediated antigen retrieval was performed in citrate buffer (pH 6.0). After the retrieval, the slides were set aside for 2 hours to cool to room temperature. Afterwards slides were washed for 5 minutes in TBS and treated with a Avidin/Biotin Blocking kit (Vector Laboratories, SP-2001). Slides were blocked with Avidin Blocking for 15 minutes, washed 3 times with TBS and finally blocked with Biotin Blocking for 15 minutes. Afterwards, the slides were incubated with the NIK antibody for 1 hour followed by washing with TBS (3 x 5 minutes) to remove residual antibody. Next, the slides were incubated with anti-rabbit IgG Alkaline Phosphatase (Sigma- Aldrich, A3687) antibody for 1 hour, washed 3 times with TBS for 5 minutes and nuclei were stained for 5 minutes with Nuclear fast Red (Sigma-Aldrich, 60700-25G). Subsequently slides were incubated in water for 5 minutes and mounted in Kaiser's glycerol gelantine (Merck).

p-STAT5 staining on human HCC liver stances

To detect levels of activated STAT5 signaling in human HCC samples, a liver carcinoma tissue array (Biomax.us, BC03013) was stained for p-STAT5 (ThermoFischer, #76-6900). The array was dehydrated at 60°C for 30 minutes, deparaffinized and heat-mediated antigen retrieval was performed in citrate buffer (pH 6.0). After the retrieval, slides were set aside for 2 hours to cool to room temperature and washed two times for 10 minutes in PBS. Subsequently, slides

were incubated in 0.3% H2O2 for 15 minutes, washed two times for 10 minutes in PBS and placed in ice cold MeOH for 5 minutes. Afterwards, slides were washed two times for 10 minutes in PBS and samples were blocked in TSA Plus cyanine 3 and Fluorescein System kit (Perkin Elmer, NEL 744001KT) for 30 minutes. Subsequently slides were incubated with diluted (1:100) primary antibody p-STAT5 (Thermo-Fischer, #76-6900) overnight at 4°C. On the next day, samples were washed with PBS + 0.1% TritonX followed by incubation with the secondary Alexa 568 goat-a-rabbit antibody (1:100 in PBS + 0.1% TritonX) for 30 minutes (Thermo Fischer, A11036). Residual secondary antibody was removed by washing 3 times for 10 minutes with PBS + 0.1% TritonX followed by incubation for 3 minutes with TSA Plus cyanine 3 and Fluorescein System kit (1:100) (Perkin Elmer, NEL753001KT). Finally, samples were washed 3 times for 10 minutes with PBS + 0.1% TritonX and mounted with vectashield(Vector Biolabs).

Murine liver samples

Sampling of murine liver tissue for histology

Tissue samples were cut from the left lateral lobe and the right medial lobe. Liver tissue was embedded either in tissue freezing medium (Leica) or placed in a cassette immersed in 10% normal buffered formalin.

In general, cryosections were placed at room temperature for 5 minutes and fixed in 4% PFA solution for 10 minutes. Residual PFA was removed by washing the slides for 10 minutes in PBS + 0.1% TritonX followed by quenching of the PFA crosslinking activity by incubation for 10 minutes in 0.3% Glycine solution. Afterwards the slides were washed for 10 minutes in PBS + 0.1% TritonX, incubated for 10 minutes in 0.03% SDS buffer and blocked for 60 min in PBS, Azide, 0.25% TritonX. Slides were incubated over night at 4°C with the respective primary antibody diluted in blocking solution. Slides were analyzed within one month after preparation to ensure proper fluorescent signal.

In general, murine liver sections were fixed in 10% NBF for 7 days at room temperature and embedded into paraffin. Tissue sections were deparaffinized and rehydrated prior to antigen unmasking using Target Retrieval Solution (Citrat Buffer pH 6.0). Slides were incubated over night at 4°C with the respective primary antibody diluted in blocking solution.

Hematoxylin and eosin staining

Overall liver tissue architecture was analyzed by H&E staining of cryosections and paraffin sections. Therefore, cryosections were placed for 1 min in ddH2O to remove tissue-freezing medium. Afterwards, sections were incubated for 2 min in Mayer's hematoxylin solution (Sigma-Aldrich, MHS32). Residual staining solution was quickly removed using ddH2O and then incubated for 15 min in tap water. Next, sections were quickly washed using ddH2O and incubated for 1 min in eosin solution (Sigma-Aldrich, HT110232,). Stained sections were washed seven times using tap water. Samples were dehydrated by incubation for 1 min in 75% ethanol, 1 min in 90 % ethanol, 1 min in 2-propanol and 1 min in xylol. Samples were mounted using Entellan (Merck, 107960) and analyzed by bright-field microscopy.

STAT5 staining

STAT5 is activated in response to a broad spectrum of ligands including IL-2, Growth Hormone and Prolactin. Upon phosphorylation of STAT5 at tyrosine residue 694 STAT5 is activated. To detect levels of activated STAT5 signaling in the liver, livers were stained for p-STAT5 (Cell signaling, #9316). Tissue sections were placed at room temperature for 5 minutes, fixed in 4% PFA solution for 10 minutes and incubated in 0.3% H2O2 for 15 minutes. Residual PFA was removed by washing the slides for 10 minutes in PBS + 0.1% TritonX followed by incubation in ice-cold MeOH for 5 minutes and two times washing in PBS + 0.1% TritonX for 10 minutes. Samples were blocked in TSA Plus cyanine 3 and Fluorescein System kit (Perkin Elmer) for 30 minutes. Subsequently slides were incubated with diluted (1:200) primary antibody p-STAT5 (Cell signaling, #9316) overnight at 4°C. On the next day, samples were washed with PBS + 0.1% TritonX followed by a 30 minute incubation with the secondary Alexa 568 goat-a-rabbit antibody (1:100 in PBS + 0.1% TritonX) (Thermo Fischer, A11036). Residual secondary antibody was removed by washing 3 times for 10 minutes with PBS + 0.1% TritonX followed by incubation for 3 minutes

with TSA Plus cyanine 3 and Fluorescein System kit (Perkin Elmer, NEL753001KT). Finally, samples were washed 3 times for 10 minutes with PBS + 0.1% TritonX.

Mac2 staining

To stain for macrophages in the white adipose tissue, slides were blocked with ROTIBlock (ROTH) for 80 minutes and washed 3 times with PBS + 0.25% TritonX. Slides were incubated overnight at 4C° with anti-MAC-2 antibodies (# CL8942AP, Cedarlane Laboratories). On the next day, samples were washed with PBS + 0.25% TritonX followed by a 60 minute incubation with the secondary goat-a-rabbit antibody HRP (1:100 in PBS + 0.1% TritonX) (Jackson Immuno Research 112-035-167).

Secondary antibody staining was performed using the EnVision Detection System (Dako) and 3,3′-diaminobenzidine as chromogenic substrate (Roche Molecular Biochemicals) according to the manufacturer's instructions

Ki67 Staining

To detect proliferating cells, liver tissue sections were stained with Ki67 antibody (abcam, #ab15580) and donkey anti-rabbit red (Jackson #711-025-152). Ki67 positive cells were counted and normalized to DAPI (Biozol) positive nuclei.

PSR

Fibrosis was evaluated based on collagen deposition on a Picro Sirius stain. Therefore, paraffin sections (7um) were processed according to manufactures instructions and stained with ab245887.

CD11b, CD45 and a-SMA staining

Inflammation was evaluated based on CD11b, CD45 and a-SMA immunohistochemistry (IHC) stain. The CD11b CD45 and a-SMA IHC was performed using a Ventana BenchMark Ultra system (Roche Diagnostics).

For the a-SMA IHC, the slides were backed at 60°C for 32 minutes, followed by deparaffinization at 72°C (Cycle 1-3:4 minutes) in Discovery Wash (Roche Diagnostics). Pretreatment was done in CC1 buffer (Roche Diagnostics) at 95°C for 24 minutes and subsequently blocked in Discovery Inhibitor (Roche Diagnostics) for 12 minutes. Slides were then incubated with primary antibody a-SMA (0.7 μg/ml; ab5694) diluted in antibody diluent for 60 minutes at 37C°. Slides incubated with antibody diluent served as negative controls.

Activated hepatic stellate cells were detected using the OmniMap anti-Rb HRP (Roche Diagnostics) at 35°C for 20 minutes. Finally, activated hepatic stellate cells were visualized by Discovery Purple kit (Roche Diagnostics) for 32 minutes. Hematoxylin II (4 minutes) and Blueing Reagent (4 minutes) (both Roche Diagnostics) were used for counterstaining.

For the CD11b IHC, the slides were backed at 60°C for 32 minutes, followed by deparaffinization at 72°C (Cycle 1-3:4 minutes) in Discovery Wash (Roche Diagnostics). Pretreatment was done in CC1 buffer (Roche Diagnostics) at 95°C for 24 minutes, blocked in Discovery Inhibitor (Roche Diagnostics) for 12 minutes and TNB (Perkin Elmer) blocking buffer for 20 minutes. Slides were then incubated with primary antibody CD11b (0,3μg/ml, ab133357) for 60 minutes at 37C°. Slides incubated with antibody diluent served as negative controls. Leukocytes were detected using the OmniMap anti-Rb HRP (Roche Diagnostics) at 35°C for 20 minutes. Finally, Leukocytes were visualized by Discovery Purple kit (Roche Diagnostics) for 32 minutes. Hematoxylin II (4 minutes) and Blueing Reagent (4 minutes) (both Roche Diagnostics) were used for counterstaining.

For the CD45 IHC, the slides were backed at 60°C for 32 minutes, followed by deparaffinization at 72°C (Cycle 1-3:4 minutes) in Discovery Wash (Roche Diagnostics). Pretreatment was done in CC1 buffer (Roche Diagnostics) at 95°C for 24 minutes, blocked in Discovery Inhibitor (Roche Diagnostics) for 12 minutes. Slides were then incubated with primary antibody CD45 (2μg/ml, ab10558) for 60 minutes at 37C°. Slides incubated with antibody diluent served as negative controls. Leukocytes were detected using the OmniMap anti-Rb HRP (Roche Diagnostics) at 35°C for 20 minutes. Finally, Leukocytes were visualized by Discovery Purple kit (Roche Diagnostics) for 32 minutes. Hematoxylin II (4 minutes) and Blueing Reagent (4 minutes) (both Roche Diagnostics) were used for counterstaining. Slides were

scanned and analyzed with Vis image analysis software (Visiopharm, Hoersholm, Denmark).

Imaging and quantification

Images were captured using a confocal Leica TCS microscope, equipped with 20x/0.75 and 40x/1.30 immersion objectives. Laser intensities for the probe channels were kept constant throughout the imaging process. Images of the liver were captured rendering approximately 5 sections per liver lobe per animal. Images were imported into Fiji (NIH), where the DAPI channel was enhanced regarding brightness and contrast, but the probe channels were left unmodified.

Statistics

To determine group size necessary for adequate statistical power, a power analysis was performed using preliminary data sets. Mice of the indicated genotype were assigned at random groups. Mouse studies were performed in a blinded fashion. Data are presented as mean ± SEM.. Outliers were removed when statistically significant, calculated by ROUT analysis. Statistical significance was calculated using GraphPad prism software using either a two- tailed unpaired Student's t test, or for the comparison between more than two conditions, a one-way or two-way ANOVA, both with Fisher's LSD test, as indicated individually. Significance was given at the level of *$P \leq 0.05$, **$P \leq 0.01$, ***$P \leq 0.001$ versus control.

REFERENCES

[1] Younossi, Z.M., et al., 2019. The global epidemiology of NAFLD and NASH in patients with type 2 diabetes: a systematic review and meta-analysis. J Hepatol 71(4):793—801.

[2] Lee, J., 2020. The obesity pandemic and the search for solutions. J Med Food 23(3):205.

[3] Adams, L.A., et al., 2005. The natural history of nonalcoholic fatty liver disease: a population-based cohort study. Gastroenterology 129(1):113—121.

[4] White, D.L., Kanwal, F., El-Serag, H.B., 2012. Association between nonalcoholic fatty liver disease and risk for hepatocellular cancer, based on systematic review. Clin Gastroenterol Hepatol 10(12):1342—1359 e2.

[5] Wolf, M.J., et al., 2014. Metabolic activation of intrahepatic CD8+ T cells and NKT cells causes nonalcoholic steatohepatitis and liver cancer via cross-talk with hepatocytes. Cancer Cell 26(4):549—564.

[6] Baffy, G., Brunt, E.M., Caldwell, S.H., 2012. Hepatocellular carcinoma in non-alcoholic fatty liver disease: an emerging menace. J Hepatol 56(6):1384—1391.

[7] Younossi, Z., et al., 2019. Nonalcoholic steatohepatitis is the fastest growing cause of hepatocellular carcinoma in liver transplant candidates. Clin Gastroenterol Hepatol 17(4):748—755 e3.

[8] Seen, T.K., et al., 2021. Clinical indicators for progression of nonalcoholic steatohepatitis to cirrhosis. World J Gastroenterol 27(23):3238—3248.

[9] Mueller, K.M., et al., 2012. Hepatic growth hormone and glucocorticoid receptor signaling in body growth, steatosis and metabolic liver cancer development. Mol Cell Endocrinol 361(1—2):1—11.

[10] Tak, P.P., Firestein, G.S., 2001. NF-kappaB: a key role in inflammatory diseases. J Clin Invest 107(1):7—11.

[11] Shih, V.F., et al., 2011. A single NFkappaB system for both canonical and non-canonical signaling. Cell Res 21(1):86—102.

[12] Wunderlich, F.T., et al., 2008. Hepatic NF-kappa B essential modulator deficiency prevents obesity-induced insulin resistance but synergizes with high-fat feeding in tumorigenesis. Proc Natl Acad Sci U S A 105(4):1297—1302.

[13] Luedde, T., et al., 2007. Deletion of NEMO/IKKgamma in liver parenchymal cells causes steatohepatitis and hepatocellular carcinoma. Cancer Cell 11(2):119—132.

[14] Maeda, S., et al., 2005. IKKbeta couples hepatocyte death to cytokine-driven compensatory proliferation that promotes chemical hepatocarcinogenesis. Cell 121(7):977—990.

[15] Nakagawa, H., et al., 2014. ER stress cooperates with hypernutrition to trigger TNF-dependent spontaneous HCC development. Cancer Cell 26(3):331—343.

[16] Pikarsky, E., et al., 2004. NF-kappaB functions as a tumour promoter in inflammation-associated cancer. Nature 431(7007):461—466.

[17] Liao, G., et al., 2004. Regulation of the NF-kappaB-inducing kinase by tumor necrosis factor receptor-associated factor 3-induced degradation. J Biol Chem 279(25):26243—26250.

[18] Sun, S.C., 2011. Non-canonical NF-kappaB signaling pathway. Cell Res 21(1): 71—85.

[19] Boutaffala, L., et al., 2015. NIK promotes tissue destruction independently of the alternative NF-kappaB pathway through TNFR1/RIP1-induced apoptosis. Cell Death Differ 22(12):2020—2033.

[20] Demchenko, Y.N., et al., 2010. Classical and/or alternative NF-kappaB pathway activation in multiple myeloma. Blood 115(17):3541—3552.

[21] Keats, J.J., et al., 2007. Promiscuous mutations activate the noncanonical NF-kappaB pathway in multiple myeloma. Cancer Cell 12(2):131—144.

[22] Saitoh, Y., et al., 2008. Overexpressed NF-kappaB-inducing kinase contributes to the tumorigenesis of adult T-cell leukemia and Hodgkin Reed-Sternberg cells. Blood 111(10):5118—5129.

[23] Thu, Y.M., et al., 2012. NF-kappaB inducing kinase (NIK) modulates melanoma tumorigenesis by regulating expression of pro-survival factors through the beta-catenin pathway. Oncogene 31(20):2580—2592.

[24] Invalid citation !!! 19-23.

[25] Xiong, Y., et al., 2018. Hepatic NF-kB-inducing kinase (NIK) suppresses mouse liver regeneration in acute and chronic liver diseases. Elife 7.

[26] Shen, H., et al., 2014. Mouse hepatocyte overexpression of NF-kappaB-inducing kinase (NIK) triggers fatal macrophage-dependent liver injury and fibrosis. Hepatology 60(6):2065—2076.

[27] Hahn, M., et al., 2016. NF-kappaB-inducing kinase is essential for B-cell maintenance in mice. Eur J Immunol 46(3):732—741.

[28] Kellendonk, C., et al., 2000. Hepatocyte-specific expression of Cre recombinase. Genesis 26(2):151—153.

[29] Boland, M.L., et al., 2019. Towards a standard diet-induced and biopsy-confirmed mouse model of non-alcoholic steatohepatitis: impact of dietary fat source. World J Gastroenterol 25(33):4904—4920.

[30] Invalid citation !!! 28.

[31] Newell, P., et al., 2008. Experimental models of hepatocellular carcinoma. J Hepatol 48(5):858—879.

[32] Barros, P., et al., 2012. Rac1 signalling modulates a STAT5/BCL-6 transcriptional switch on cell-cycle-associated target gene promoters. Nucleic Acids Res 40(16):7776—7787.

[33] Zhang, Y., Laz, E.V., Waxman, D.J., 2012. Dynamic, sex-differential STAT5 and BCL6 binding to sex-biased, growth hormone-regulated genes in adult mouse liver. Mol Cell Biol 32(4):880—896.

[34] Lin, G., et al., 2014. Reciprocal occupancy of BCL6 and STAT5 on Growth Hormone target genes: contrasting transcriptional outcomes and promoter-specific roles of p300 and HDAC3. Mol Cell Endocrinol 395(1—2):19—31.

[35] Csepregi, A., et al., 2010. Promoter methylation of CDKN2A and lack of p16 expression characterize patients with hepatocellular carcinoma. BMC Cancer 10:317.

[36] Fornari, F., et al., 2008. MiR-221 controls CDKN1C/p57 and CDKN1B/p27 expression in human hepatocellular carcinoma. Oncogene 27(43):5651—5661.

[37] Yu, J.H., et al., 2010. The transcription factors signal transducer and activator of transcription 5A (STAT5A) and STAT5B negatively regulate cell proliferation through the activation of cyclin-dependent kinase inhibitor 2b (Cdkn2b) and Cdkn1a expression. Hepatology 52(5):1808—1818.

[38] Friedbichler, K., et al., 2012. Growth-hormone-induced signal transducer and activator of transcription 5 signaling causes gigantism, inflammation, and premature death but protects mice from aggressive liver cancer. Hepatology 55(3):941—952.

[39] Hosui, A., et al., 2017. Signal transducer and activator of transcription 5 plays a crucial role in hepatic lipid metabolism through regulation of CD36 expression. Hepatol Res 47(8):813—825.

[40] Shipley, J.M., Waxman, D.J., 2004. Simultaneous, bidirectional inhibitory crosstalk between PPAR and STAT5b. Toxicol Appl Pharmacol 199(3):275—284.

[41] Sasaki, Y., et al., 2008. NIK overexpression amplifies, whereas ablation of its TRAF3-binding domain replaces BAFF:BAFF-R-mediated survival signals in B cells. Proc Natl Acad Sci U S A 105(31):10883—10888.

[42] Sanz, A., et al., 2011. Analysis of Jak2 catalytic function by peptide micro-arrays: the role of the JH2 domain and V617F mutation. PLoS One 6(4): e18522.

[43] Robertson, S.A., et al., 2009. Regulation of Jak2 function by phosphorylation of Tyr317 and Tyr637 during cytokine signaling. Mol Cell Biol 29(12):3367—3378.

[44] Adamek, A., Kasprzak, A., 2018. Insulin-like growth factor (IGF) system in liver diseases. Int J Mol Sci 19(5).

[45] Rehem, R.N., El-Shikh, W.M., 2011. Serum IGF-1, IGF-2 and IGFBP-3 as parameters in the assessment of liver dysfunction in patients with hepatic cirrhosis and in the diagnosis of hepatocellular carcinoma. Hepato-Gastroenterology 58(107—108):949—954.

[46] Wang, J., et al., 2017. Serum insulin-like growth factor-1 and its binding protein 3 as prognostic factors for the incidence, progression, and outcome of hepatocellular carcinoma: a systematic review and meta-analysis. Oncotarget 8(46):81098—81108.

[47] Carotti, S., et al., 2018. Impairment of GH/IGF-1 Axis in the liver of patients with HCV-related chronic hepatitis. Horm Metab Res 50(2):145—151.

[48] Invalid citation !!! 43-46.

[49] Mao, Y., et al., 1999. Endotoxin-induced inhibition of growth hormone receptor signaling in rat liver in vivo. Endocrinology 140(12):5505—5515.

[50] Yumet, G., et al., 2002. Tumor necrosis factor mediates hepatic growth hormone resistance during sepsis. Am J Physiol Endocrinol Metab 283(3): E472—E481.

[51] Lang, C.H., Hong-Brown, L., Frost, R.A., 2005. Cytokine inhibition of JAK-STAT signaling: a new mechanism of growth hormone resistance. Pediatr Nephrol 20(3):306—312.

[52] Barclay, J.L., et al., 2011. GH-dependent STAT5 signaling plays an important role in hepatic lipid metabolism. Endocrinology 152(1):181—192.

[53] Mueller, K.M., et al., 2011. Impairment of hepatic growth hormone and glucocorticoid receptor signaling causes steatosis and hepatocellular carcinoma in mice. Hepatology 54(4):1398—1409.

[54] Argetsinger, L.S., et al., 1993. Identification of JAK2 as a growth hormone receptor-associated tyrosine kinase. Cell 74(2):237—244.

[55] Han, Y., et al., 1996. Participation of JAK and STAT proteins in growth hormone-induced signaling. J Biol Chem 271(10):5947—5952.

[56] Carter-Su, C., Rui, L., Herrington, J., 2000. Role of the tyrosine kinase JAK2 in signal transduction by growth hormone. Pediatr Nephrol 14(7):550—557.

[57] Zhao, L., et al., 2009. A JAK2 interdomain linker relays Epo receptor engagement signals to kinase activation. J Biol Chem 284(39):26988—26998.

[58] Ungureanu, D., et al., 2011. The pseudokinase domain of JAK2 is a dual-specificity protein kinase that negatively regulates cytokine signaling. Nat Struct Mol Biol 18(9):971—976.

[59] Jones, A.V., et al., 2005. Widespread occurrence of the JAK2 V617F mutation in chronic myeloproliferative disorders. Blood 106(6):2162—2168.

[60] Skoda, R.C., Duek, A., Grisouard, J., 2015. Pathogenesis of myeloproliferative neoplasms. Exp Hematol 43(8):599—608.

[61] Kralovics, R., et al., 2005. A gain-of-function mutation of JAK2 in myeloproliferative disorders. N Engl J Med 352(17):1779—1790.

[62] Baxter, E.J., et al., 2005. Acquired mutation of the tyrosine kinase JAK2 in human myeloproliferative disorders. Lancet 365(9464):1054—1061.

[63] Kovanen, P.E., et al., 2000. Regulation of Jak2 tyrosine kinase by protein kinase C during macrophage differentiation of IL-3-dependent myeloid progenitor cells. Blood 95(5):1626—1632.

[64] Ishida-Takahashi, R., et al., 2006. Phosphorylation of Jak2 on Ser(523) inhibits Jak2-dependent leptin receptor signaling. Mol Cell Biol 26(11):4063—4073.

[65] Mazurkiewicz-Munoz, A.M., et al., 2006. Phosphorylation of JAK2 at serine 523: a negative regulator of JAK2 that is stimulated by growth hormone and epidermal growth factor. Mol Cell Biol 26(11):4052—4062.

[66] Wilhelm, A., et al., 2016. Interaction of TWEAK with Fn14 leads to the progression of fibrotic liver disease by directly modulating hepatic stellate cell proliferation. J Pathol 239(1):109—121.

[67] Gao, Q., et al., 2019. Integrated proteogenomic characterization of HBV-related hepatocellular carcinoma. Cell 179(5):1240.